

1
2
3
4
5
6
7
8
9
10
11
12
13
14
15
16
17

The Frictional-Viscous Transition in Experimentally Deformed Granitoid Fault Gouge

W. Zhan¹, A. R. Niemeijer², A. Berger¹, N. Nevskaya¹, C. J. Spiers², M. Herwegh¹

¹Institute of Geological Sciences, University of Bern, Bern, Switzerland.

²Department of Earth Sciences, Utrecht University, Utrecht, the Netherlands.

Corresponding author: Weijia Zhan (weijia.zhan@unibe.ch)

Key Points:

- The frictional-viscous transition in granitoid gouges is promoted by increasing temperature and decreasing velocity.
- The transition involves forming a dense, ultrafine-grained principal slip zone where dissolution-precipitation creep operates.
- This temperature-, rate- and grain size-sensitive creep mechanism greatly weakens the crust at depth >7 km depending on geothermal gradient.

18 **Abstract**

19 In crustal faults dominated by granitoid gouges, the frictional-viscous transition marks a
20 significant change in strength constraining the lower depth limit of the seismogenic zone.
21 Dissolution-precipitation creep (DPC) may play an important role in initiating this transition,
22 especially within polymineralic materials. Yet, it remains unclear to what extent DPC
23 contributes to the weakening of granitoid gouge materials at the transition. Here we
24 conducted sliding experiments on wet granitoid gouges to large displacement (15 mm), at an
25 effective normal stress and pore fluid pressure of 100 MPa, at temperatures of 20-650°C, and
26 at sliding velocities of 0.1-100 $\mu\text{m/s}$, which are relevant for earthquake nucleation. Gouge
27 shear strengths were generally ~ 75 MPa even at temperatures up to 650°C and at velocities $>$
28 $1 \mu\text{m/s}$. At velocities $\leq 1 \mu\text{m/s}$, strengths decreased at temperatures $\geq 450^\circ\text{C}$, reaching a
29 minimum of 37 MPa at the highest temperature and lowest velocity condition.
30 Microstructural observations showed that, as the gouges weakened, the strain localized into
31 thin, dense, and ultrafine-grained ($\leq 1 \mu\text{m}$) principal slip zones, where nanopores were
32 located along grain contacts and contained minute biotite-quartz-feldspar precipitates.
33 Though poorly constrained, the stress sensitivity exponent n decreased from ≥ 17 at 20°C to
34 ~ 2 at 650°C at the lowest velocities. These findings suggest that high temperature, slow
35 velocity and/or small grain sizes promote DPC-accommodated granular flow over cataclastic
36 frictional granular flow, leading to the observed weakening and strain localization. Field
37 observations together with extrapolation suggest that DPC-induced weakening occurs at
38 depths of 7-20 km depending on geothermal gradient.

39 **Plain Language Summary**

40 Below the Earth's surface, rocks usually undergo a change in strength and deformation
41 behavior as they reach deeper crustal levels, transitioning from strong and brittle behavior in
42 the upper crust, to weak and viscous near the middle crust. This change, known as the
43 frictional-viscous transition, defines the limit in depth where major earthquakes can occur.
44 Some evidence from nature and laboratory experiments suggest that deformation by
45 dissolution-precipitation creep (DPC or "pressure solution") may play an important role in
46 triggering this transition. However, these assumptions lack adequate verification and
47 comprehensive understanding. Here, we conducted laboratory tests across a wide range of
48 temperatures and deformation rates in order to reconstruct the frictional-viscous transition in
49 granitoid rocks, one of the most common rock type in the upper to middle continental crust.
50 We found that granitoid gouges started to weaken and became viscous when being deformed

51 at higher temperatures and lower deformation rates. As the rock became weaker, deformation
52 localized in a distinct layer called the principal slip zone. This is very fine-grained and
53 contains tiny pores filled with many newly precipitated minerals, which proves active DPC.
54 In nature, activation of DPC could trigger the frictional-viscous transition at shallower crustal
55 depths than otherwise expected.

56 **1 Introduction**

57 Granitoid or granitic fault gouge is a type of non-cohesive fault rock that consist
58 predominantly of quartz, albite and orthoclase (Barbarin, 1999; Sammis et al., 1987).
59 Observations of natural fault zones suggest deformation often localizes into a thin layer of
60 non-cohesive granitoid fault rocks in the crystalline part of the continental crust, at upper to
61 middle crustal depths (Baumberger et al., 2022; Berger et al., 2017; Wehrens et al., 2016).
62 Therefore, the mechanical behavior of these granitoid gouges is highly relevant for
63 determining the rheology of crustal fault zones. The frictional-viscous transition in these
64 gouges is of great importance, as it not only marks a pronounced change in rheological
65 properties of the Earth's lithosphere, but also helps to constrain the lower boundary of the
66 seismogenic zone, where large-magnitude earthquakes normally originate (Evans et al., 1990;
67 Scholz, 1998; Sibson, 1982; Tse & Rice, 1986).

68 In the classical crustal rheological profile, the frictional-viscous transition extends
69 over a depth range of several kilometers, serving as a bridge between predominantly
70 frictional behavior in the upper crust and viscous behavior in the lower crust (Bürgmann &
71 Dresen, 2008; Burov, 2011; Goetze & Evans, 1979; Kohlstedt et al., 1995; Paterson & Wong,
72 2005). The strength of the upper crust typically increases linearly with depth, characterized
73 by a constant slope represented by friction coefficients of ~0.6-0.85, often referred to as
74 Byerlee's law (J. Byerlee, 1978; Labuz & Zang, 2012). Within the upper crust, frictional
75 sliding occurs along preexisting fault planes, with low temperature and strain rate sensitivity.
76 In contrast, the strength of the lower crust generally decreases with increasing depth. This
77 behavior is often described by the thermally activated, power-law flow of monomineralic
78 quartz or feldspar, which are the most abundant rock forming minerals at this crustal level. In
79 the case of these end-member minerals, deformation is thought to be mainly controlled by
80 dislocation creep and dynamic recrystallization processes (Rutter & Brodie, 2004b; Rybacki
81 & Dresen, 2004). Deformation at the frictional-viscous transition is usually considered as a
82 combination of the frictional and creep mechanisms that separately govern the deformation of
83 the upper and the lower crust. However, the widespread occurrence of stylolites,

84 slickenfibres, veining, grain scale overgrowths and truncated grain-grain contacts, found in
85 exhumed mid-crustal fault zones (Gratier et al., 2023; Hickman et al., 1995; Wassmann &
86 Stöckhert, 2013, and references therein), indicate that apart from the classical frictional and
87 creep mechanisms, dissolution-precipitation creep may play an important role particularly in
88 the case of polymineralic faults. It is also known as pressure solution (Gratier et al., 2013;
89 Spiers et al., 1990) or viscous granular creep (Paterson 1995; Stünitz 1998).

90 Dissolution-precipitation creep (DPC) is a fluid-assisted deformation mechanism
91 involving three processes: first, material is dissolved at grain contacts with relatively high
92 normal stress concentrations, then transported away from the contacts by diffusive mass
93 transport process, and finally precipitated at low stress sites (Gratier et al., 2013; Rutter,
94 1983; X. Zhang & Spiers, 2005). Under conditions where fluids are present, DPC is promoted
95 and accelerated by the presence of fine grain size, polymineralic composition, moderate
96 temperatures and slow strain rates (de Meer & Spiers, 1997; Rutter, 1983; Visser et al.,
97 2012). These conditions align well with those found in permeable mid-crustal fault zones,
98 suggesting that DPC may indeed represent a dominant deformation mechanism within the
99 frictional-viscous transition. DPC is typically known to play a crucial role in compaction,
100 sealing and healing of fault rocks during the interseismic period between individual
101 earthquake events (Nakatani & Scholz, 2004; Niemeijer et al., 2002; Schwichtenberg et al.,
102 2022). More importantly, several studies have demonstrated that this mechanism may also
103 reduce the strength of fault rocks at the frictional-viscous transition, especially in fault rocks
104 that contain fine-grained phyllosilicates (Bos & Spiers, 2001; Kirkpatrick et al., 2021) or
105 albite (Okuda et al., 2023). Yet, it remains unclear to what extent DPC contributes to the
106 weakening of granitoid gouge materials at the frictional-viscous transition.

107 Many laboratory experiments conducted under hydrothermal conditions have
108 investigated the frictional-viscous transition and associated deformation processes in the case
109 of different rock compositions, such as pure quartz gouge (Hirth & Tullis, 1992, 1994), albite
110 gouge (Tullis & Yund, 1992), and granitoids (Blanpied et al., 1995; Lei, Niemeijer, et al.,
111 2022; Mitchell et al., 2016; Simpson, 1985; Tullis & Yund, 1980). These experimental
112 studies have demonstrated that the frictional-viscous transition occurs in a range of increasing
113 temperature and/or decreasing sliding velocity, which typically is expressed by temperatures
114 of around 350-450°C under a velocity range of 0.01-1 $\mu\text{m/s}$. For monomineralic aggregates
115 such as quartz gouge, DPC has been demonstrated to play an important role in weakening the
116 gouges (Niemeijer et al., 2008). A more pronounced weakening effect was observed in

117 granitoid gouges due to the addition of water, emphasizing the important role of fluid-assisted
118 deformation mechanisms, such as DPC, in initiating the frictional-viscous transition in
119 polymineralic aggregates (Blanpied et al., 1995; Griggs, 1967; Tullis & Yund, 1980).
120 However, these experiments were confined to small shear strains ($\gamma \approx 4-7$), and the
121 microstructural investigations were limited to either optical microscopy or transmission
122 electron microscopy scales. These constraints hinder a comprehensive understanding of the
123 role of DPC on weakening at the frictional-viscous transition, as its processes are mainly
124 observable at intermediate grain-scales.

125 In this study, we aim to replicate the frictional-viscous transition in the case of fine-
126 grained granitoid gouges in order to gain more profound knowledge of the associated
127 deformation mechanisms. We conducted sliding experiments on wet granitoid gouges to large
128 displacement (15 mm) under hydrothermal conditions (20-650°C, 100 MPa pore fluid
129 pressure, and effective normal stress) and at sliding velocities (0.1-100 $\mu\text{m/s}$) relevant for
130 earthquake nucleation. Microstructures of deformed samples were quantitatively analyzed at
131 a variety of scales, using methods allowing observation from the mm down to the nm range.
132 The laboratory measurements of gouge strengths were further extrapolated to natural
133 conditions. Together, our results demonstrate that notable weakening at the frictional-viscous
134 transition is accompanied by intense strain localization, elimination of fracture arrays and the
135 formation of nanopores at grain contact surfaces that contained tiny precipitated biotite
136 flakes. In terms of deformation mechanisms, cataclastic frictional granular flow is gradually
137 replaced by DPC-accommodated viscous granular flow at temperatures above 450°C, sliding
138 velocities below 1 $\mu\text{m/s}$, and/or mean grain size below 1 μm .

139 **2 Materials and Methods**

140 **2.1. Starting material**

141 The investigated “gouges” were produced from a granitoid ultramylonite that was
142 drilled and cored from a ductile shear zone inside the Nagra Grimsel Test Site (GTS), an
143 underground rock laboratory located near Grimsel Pass in the Aar Massif, Central
144 Switzerland (46°35'27"N, 8°19'17"E; e.g. Schneeberger et al., 2017). The collected sample
145 was disaggregated in a step-wise procedure to simulate non-cohesive gouge-like powders.
146 They were first crushed into large fragments by electrical fragmentation, which is based on
147 high-voltage discharges (SELFRAG[®]: www.selfrag.com; Giese et al., 2010; Zwingmann et
148 al., 2017), then further milled into powders with a McCrone micronizing mill for less than 1

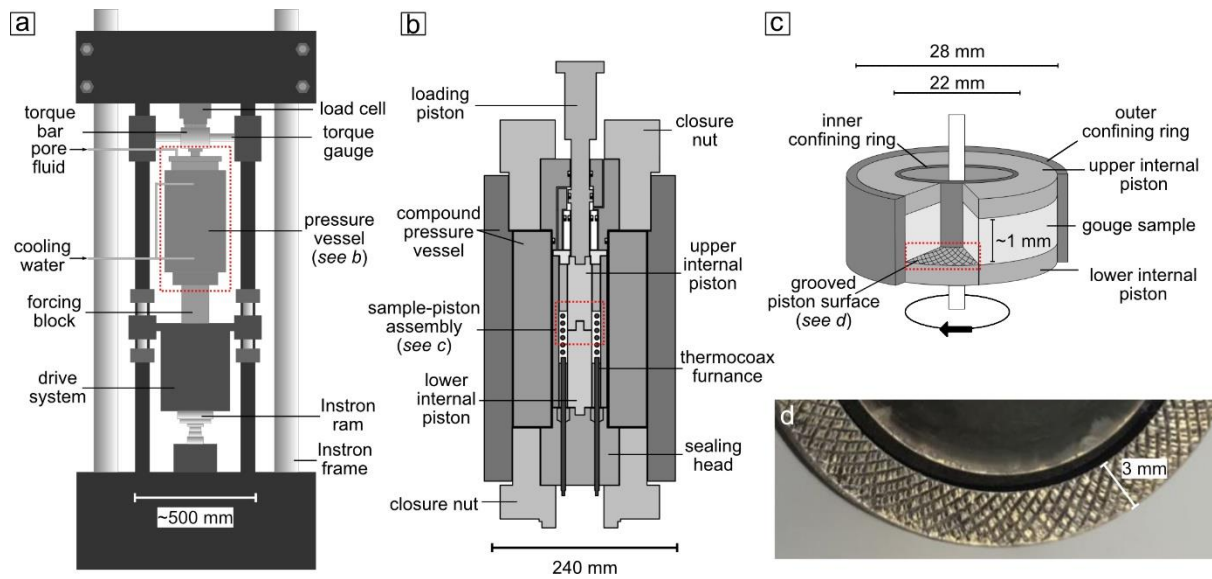
149 minute (Behnsen & Faulkner, 2011). Fragments that remained large were manually ground
150 with a mortar and pestle and subsequently wet sieved to obtain a grain size fraction smaller
151 than 125 μm . All of the disaggregated material was collected and dried in an oven at $\sim 40^\circ\text{C}$
152 for at least 48 h and stored in sealed containers at room temperature and ambient humidity.

153 To determine the mineralogical composition and particle size distribution, powders
154 were analyzed using X-ray Powder Diffraction (XRD) and a laser particle-size
155 diffractometer, respectively (supporting information, Text S1). XRD results show that the
156 starting material has a typical granitoid composition, being composed of quartz (37 wt.%),
157 albite (38 wt.%), orthoclase (11 wt.%), biotite (8 wt.%) and epidote (6 wt.%). Particle size
158 analysis shows a log-normal distribution, with a mean grain size of 56 μm and a standard
159 deviation of 47 μm .

160 2.2. Experimental techniques

161 Rock deformation experiments were conducted in a hydrothermal ring shear
162 apparatus, installed at the HPT lab at Utrecht University (see details in den Hartog et al.,
163 2012; Niemeijer et al., 2008). In this apparatus, an internally heated pressure vessel and a
164 rotary drive system are installed inside an Instron loading frame (Figure 1a). Within the
165 pressure vessel, the pore fluid pressure is controlled using a hand pump. The added fluid is
166 deionized water. The effective normal stress (resolution ± 0.05 MPa) is transmitted to the
167 sample through a pressure-compensated loading piston using the Instron ram (Figure 1a). The
168 sample is heated to the desired temperature (resolution $\pm 0.5^\circ\text{C}$) using a coiled thermocoax
169 furnace surrounding the sample-piston assembly. Sample temperatures are measured using a
170 K-type thermocouple installed ~ 5 mm away from the sample layer. For each experiments, a
171 ~ 1.5 mm thick gouge layer was sandwiched between two internal René-41[®] superalloy
172 pistons in the sample-piston assembly (Figure 1c). The internal pistons are roughened with
173 ~ 0.2 mm deep, cross-cut grooves to increase the grip between the sample powder and piston
174 surfaces (Figure 1d). The gouge is confined with inner (22 mm diameter) and outer confining
175 rings (28 mm diameter) which were coated with Molykote[®] (MoS_2) antifriction lubricant to
176 reduce the wall friction between sample and the confining rings (Verberne et al., 2015). The
177 resulting shear stress is externally measured using the torque gauges mounted on the torque
178 bar at the top of the pressure vessel (resolution ± 0.006 MPa). Shear displacement is measured
179 using a potentiometer installed at the bottom-forcing block (resolution ± 0.001 mm).

180



181

182 **Figure 1.** (a) Schematic diagram of hydrothermal ring shear apparatus showing the pressure
 183 vessel and fluid lines; (b) Cross section of the compound pressure vessel, modified after den
 184 Hartog and Spiers (2013); (c) Schematic diagram of sample assembly; (d) Photograph of the
 185 grooved piston surface.

186 In each experiment, the desired temperature and pore fluid pressure were applied
 187 within ~30 min of installing the sample in the apparatus. After equilibrating for at least 45
 188 min, the effective normal stress was applied to the sample, and then the rotary driving system
 189 was switched on. Upon completion of the experiment, shear stress, effective normal stress,
 190 temperature, and pore fluid pressure were sequentially decreased. Temperature and pore fluid
 191 pressure were adjusted to atmospheric conditions in a stepwise procedure to avoid pore fluid
 192 boiling. The experiment termination process took ~30 min. During the experiment, signals
 193 including shear displacement, torque, temperature, axial displacement and load, pore fluid
 194 pressure, and rotational drive velocity were continuously recorded using a 18-bit A/D
 195 converter and an acquisition rate of 900 Hz, which was averaged and logged at frequencies of
 196 1-100 Hz, depending on sliding velocities.

197 Sixteen experiments in total were conducted at an effective normal stress of 100 MPa
 198 and a pore fluid pressure of 100 MPa applying ~15 mm displacement (shear strain of ~23).
 199 They are subdivided into three groups based on the applied sliding velocities of $V = 100, 1,$
 200 $0.1 \mu\text{m/s}$ (Table 1). In the first group, gouges were sheared at a constant sliding velocity of V
 201 $= 100 \mu\text{m/s}$ and temperatures ranging from 20°C to 650°C , in order to study the effect of
 202 temperature on the strength of the gouge. The second and the third groups are identical to the
 203 first group, except that the applied sliding velocity was, respectively, set at $V = 1 \mu\text{m/s}$ and V

204 = 0.1 $\mu\text{m/s}$ to study how fault slip rate influences the strength of gouge samples. To prevent
205 melting, the highest temperature and pore fluid pressure conditions explored were
206 deliberately chosen to be well below the H_2O -saturated melting curve for granitoid system
207 ($T= 690^\circ\text{C}$ at 200 MPa, Johannes, 1984; Lamadrid et al., 2014). After reaching the desired
208 displacement, each sample was quickly removed from the apparatus and dried in an oven. In
209 some experiments, samples underwent shearing and were then held at the designated
210 temperature and pressure for a specific duration (listed as t_{hold} in Table 1), followed by
211 unloading. Static grain growth of grains during the hold duration may influence
212 microstructures, particularly the absolute grain sizes of sheared samples. To investigate these
213 effects, we conducted additional experiments with identical displacement, sliding velocity
214 and zero hold duration ($t_{\text{hold}} = 0$ h).

215 During data processing, the recorded torque was corrected for seal friction to obtain
216 the shear stress (τ), while the potentiometer displacement (D) was corrected for elastic
217 distortion. We define the yield point as the point of the minimum second derivative of the
218 shear stress-displacement curve. In the initial loading stage leading up to the yield point thus
219 defined, shear stresses showed a near-linear increase with displacement, appearing as a
220 straight line in the stress-displacement curve. Beyond the yield point, the rate of increase in
221 shear stresses decreased, i.e. the slope of the stress-displacement curves decreases, ultimately
222 approaching a steady state. The yield point shear stresses (τ_{yd}) were calculated as the average
223 of measurements taken over a 1 mm displacement interval beyond the yield point
224 displacement value. The (near) steady-state shear stresses (τ_{ss}) were calculated in a similar
225 way, but only when a total displacement of 15 mm was achieved. For experiment u1150 with
226 a total displacement less than 15 mm, τ_{ss} was picked up at a displacement of ~ 13 mm. The
227 difference between τ_{ss} and τ_{yd} represents the extent of shear stress changes ($\Delta\tau$), calculated
228 as $\Delta\tau = \tau_{ss} - \tau_{yd}$.

229 **Table 1.** List of experiments, conditions and key data. All experiments were conducted under
 230 an effective normal stress of 100 MPa and a pore fluid pressure of 100 MPa (normal stress is
 231 200 MPa). T : temperature, V : sliding velocity, D : displacement, t_{hold} : time for sample being
 232 hold at applied P-T conditions before unload, τ_{yd} : yield point shear stress selected at the
 233 point of the minimum second derivative of shear stress-displacement curve, τ_{ss} : (near)
 234 steady-state shear stress selected at displacements of ~ 15 mm, $\Delta\tau = \tau_{ss} - \tau_{yd}$, μ_{ss} : apparent
 235 friction coefficient at (near) steady-state, calculated as $\mu_{ss} = \tau_{ss}/\sigma_n^{eff}$ by ignoring cohesion.

Experiments	T (°C)	V ($\mu\text{m/s}$)	D (mm)	t_{hold} (h)	τ_{yd} (MPa)	τ_{ss} (MPa)	$\Delta\tau$ (MPa)	μ_{ss} (-)
$V = 100 \mu\text{m/s}$								
u1051	20	100	15.08	0.0	56.69	74.50	17.81	0.75
u1049	200	100	15.11	1.4	65.01	73.58	8.57	0.74
u1052	450	100	15.10	1.1	59.96	77.40	17.44	0.77
u1059	650	100	15.47	0.5	54.81	81.51	26.70	0.82
$V = 1 \mu\text{m/s}$								
u1038	20	1	15.98	10.0	68.97	81.11	12.14	0.81
u908	200	1	15.60	0.0	56.60	75.41	18.81	0.75
u909	450	1	15.10	0.1	57.79	73.04	15.25	0.73
u1154	650	1	16.25	0.0	59.61	67.83	8.22	0.68
u913	650	1	15.60	12.0	64.34	49.78	-14.56	0.50
u1060	650	1	17.10	41.9	62.03	63.94	1.91	0.64
$V = 0.1 \mu\text{m/s}$								
u1157	20	0.1	15.59	0.0	56.31	65.82	9.51	0.66
u1153	200	0.1	15.49	0.0	54.56	65.84	11.28	0.66
u1151	450	0.1	15.50	0.0	68.73	73.56	4.83	0.74
u1150	650	0.1	13.10	0.0	73.21	49.70	-23.51	0.50
u1175	650	0.1	15.49	2.0	63.73	43.08	-20.65	0.43
u910	650	0.1	19.80	9.6	60.09	37.27	-22.82	0.37

236 2.3. Analytical methods

237 At the end of each experiment, we obtained a ring-shaped gouge layer with
 238 dimensions of ~ 3 mm in width and ~ 0.7 mm in thickness. Upon drying and disassembling,
 239 the deformed gouges often split into several fragments. We carefully selected relatively thick
 240 fragments for microstructural imaging, assuming their microstructures are representative of
 241 the entire sample. The fragments from each experiment were subjected to two different
 242 treatments: some were air-impregnated with an epoxy resin, while others were fixed to
 243 carbon SEM stubs with no impregnation. For the air-impregnated samples, sectioning was

244 performed in a plane normal to the shear plane and ~2 mm tangential to the centrally
245 inscribed circle (22 mm diameter), followed by a 10 nm thick carbon coating. Microstructural
246 consistency was confirmed across different sectioned distances from the inscribed circle.
247 Backscatter images of the sectioned sample were collected and stitched using a ZEISS EVO
248 50 scanning electron microscope (SEM) at 20 kV and 0.5-1.5 nA. These stitched images
249 provided an overview of the microstructure with the aim to cover the entire thickness of the
250 final gouge layer. Close-up images were obtained using a ZEISS Gemini SEM 450 (FEG-
251 SEM) operating at 10 kV and 300 pA. As for the fragments on carbon SEM stubs, backscatter
252 images of broken surfaces were obtained using the FEG-SEM operating at 5 kV and 100 pA
253 to enable investigation of grain boundary morphologies.

254 BSE images were processed using the interactive machine-learning tool ilastik, and
255 then quantitatively analyzed using ImageJ. A summary of image analysis workflow can be
256 found in Text S2 of the supporting information. Based on the processed images, we classified
257 four distinct objects types: ‘clasts’, ‘matrix’, ‘pores’ and ‘cracks’. ‘Clasts’ refers to particles
258 larger than $1 \mu\text{m}^2$ (~120 pixel²), while ‘matrix’ refers to all particles smaller than $1 \mu\text{m}^2$.
259 ‘Pores’ are isolated openings, and ‘cracks’ refers to interconnected (sub)planar openings,
260 which presumably resulted from the unloading of the experiments. Two microstructural
261 features were quantitatively characterized, including the grain size distribution of clasts, as
262 well as the relative area proportion between clast, matrix and porosity (also referred to as
263 clast:matrix:porosity ratio). For the grain size distribution, the area-weighted diameter
264 ($d_i, \mu\text{m}$) was calculated using the measured area ($A_i, \mu\text{m}^2$) of each clast, according to the
265 formula below (Berger et al., 2011):

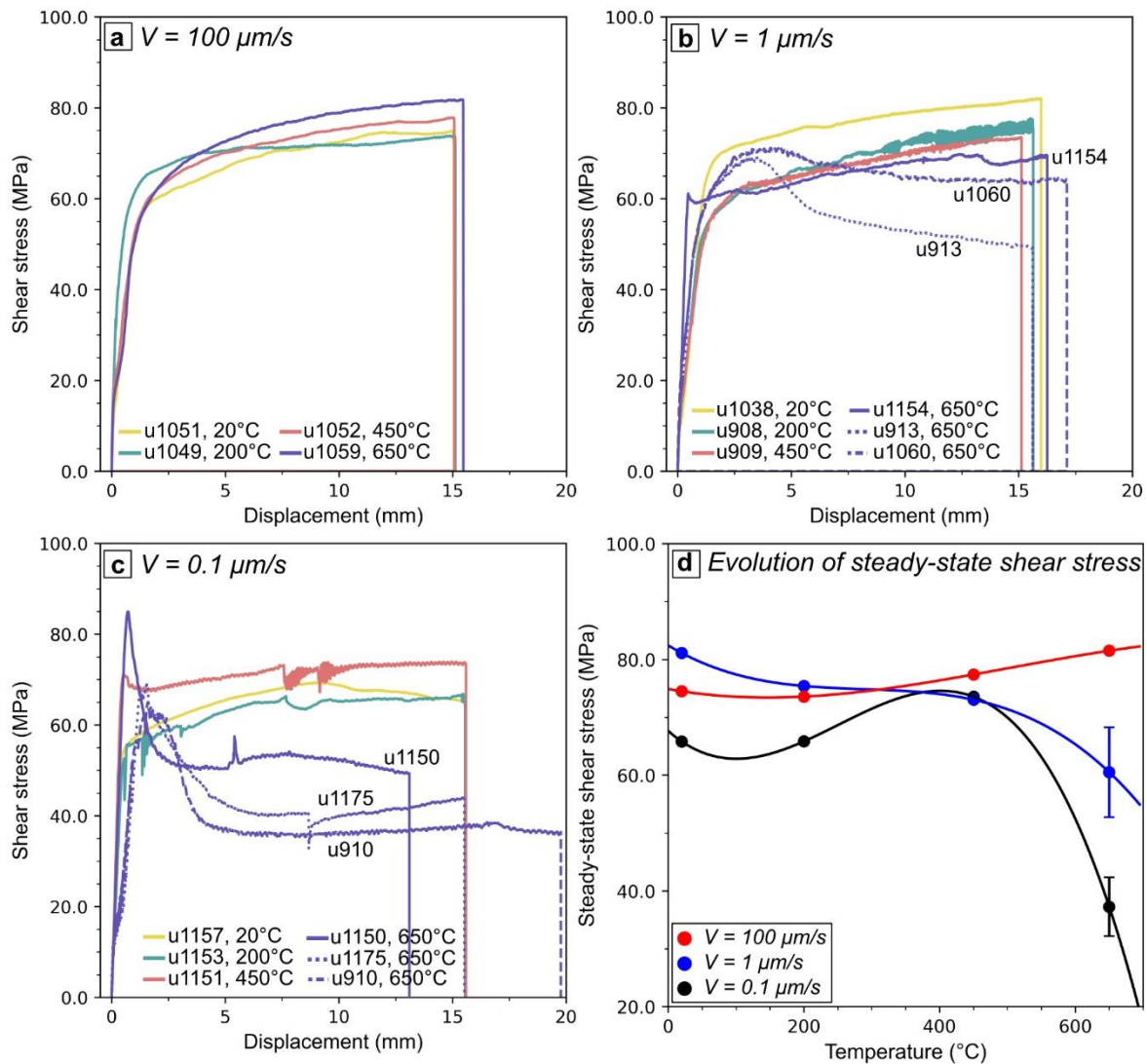
$$266 \quad d_i = 2 * \sqrt{\frac{A_i}{\pi}} \quad (1)$$

267 **3 Results**

268 **3.1. Mechanical data**

269 Diagrams of shear stress (τ) against displacement (D) are shown in Figure 2 for
270 different sliding velocities ($V = 100, 1, 0.1 \mu\text{m/s}$) and temperatures ($T = 20, 200, 450, 650^\circ\text{C}$).
271 Despite some variability, all experiments showed a steep, near-linear increase in shear stress,
272 reaching the yield point at $\tau_{yd} = \sim 70 \text{ MPa}$ within the first 1-2 mm displacements. As
273 displacements continued, shear stresses either increased (displacement-hardening) or started
274 to decrease (displacement-weakening) until gradually approaching steady state (τ_{ss}). The

275 extent of shear stress changes ($\Delta\tau$) between yield point and the steady state varied from a
 276 negative change of $\Delta\tau = -24$ MPa for samples that underwent displacement weakening, to a
 277 positive change of $\Delta\tau = +27$ MPa for those with displacement hardening. Both the applied
 278 temperatures and sliding velocities influenced the sign of shear stress changes (displacement-
 279 hardening or displacement-weakening), the extent of shear stress changes ($\Delta\tau$), as well as the
 280 stability of sliding (stable or unstable). Aforementioned key data are listed in Table 1.



281 **Figure 2.** Plots of shear stress (τ) against shear displacement (D), showing data from
 282 experiments at (a) $V = 100 \mu\text{m/s}$, (b) $V = 1 \mu\text{m/s}$, and (c) $V = 0.1 \mu\text{m/s}$. See Table 2 for a list
 283 of conditions applied in these experiments. (d) Steady-state shear stress (τ_{ss}) plotted as a
 284 function of temperature (T) and sliding velocity (V). Lines are interpreted trends.
 285

286 In the case of gouges sheared at a sliding velocity of $V = 100 \mu\text{m/s}$, samples sheared
 287 at various temperatures consistently showed stable sliding, continuous displacement-
 288 hardening, eventually reaching $\tau_{ss} = \sim 75$ MPa (Figure 2a). The extent of shear stress increase

289 exhibited no discernible dependency on temperature. In comparison, for gouges subjected to
290 a medium sliding velocity of $V = 1 \mu\text{m/s}$, temperatures showed a pronounced influence on the
291 type of shear stress changes and the stability of sliding (Figure 2b). At lower temperatures of
292 $T = 20\text{-}450^\circ\text{C}$ and in one experiment (u1154) at $T = 650^\circ\text{C}$, these samples were characterized
293 by displacement-hardening with $\tau_{ss} = \sim 75 \text{ MPa}$. As temperatures increased to $T = 650^\circ\text{C}$, the
294 samples showed a distinctive behavior, with a short region of displacement-hardening in the
295 first 2 mm displacement, followed by displacement-weakening towards $\tau_{ss} = \sim 50\text{-}64 \text{ MPa}$.
296 Only experiments conducted at temperatures between 200 and 450°C showed unstable sliding
297 behavior, which often occurred as stick-slip events. In comparison, gouges subjected to slow
298 shearing at $V = 0.1 \mu\text{m/s}$ exhibited a temperature-dependent behavior similar to those sheared
299 at $V = 1 \mu\text{m/s}$. However, for those sheared at $T = 650^\circ\text{C}$, τ_{ss} was $\sim 37\text{-}50 \text{ MPa}$ and a shorter
300 critical displacement (1-3 mm) was needed for the transition from displacement-hardening to
301 weakening behavior (Figure 2c). Note that the limited reproducibility of experiments
302 conducted at $T = 650^\circ\text{C}$ and $V = 0.1\text{-}1 \mu\text{m/s}$ is probably caused by fluctuations in pore fluid
303 pressure applied during experiments (see supporting information Figure S3).

304 To highlight the influence of temperature and sliding velocity on the strength of the
305 granitoid gouge, we plot the steady-state shear stress (τ_{ss}) against temperature in Figure 2d
306 for the three investigated sliding velocities ($V = 100, 1, 0.1 \mu\text{m/s}$). Gouges sheared at $V = 100$
307 $\mu\text{m/s}$ showed consistently high steady-state shear stresses that progressively increased with
308 elevated temperatures, from $\tau_{ss} = 74 \text{ MPa}$ at 20°C to $\tau_{ss} = 82 \text{ MPa}$ at 650°C . In contrast,
309 gouges sheared at lower velocities of $V = 1$ and $0.1 \mu\text{m/s}$ exhibited mostly temperature-
310 insensitive shear stresses at $T \leq 450^\circ\text{C}$ but showed significant weakening at $T = 650^\circ\text{C}$.
311 Specifically, for gouges sheared at $V = 1 \mu\text{m/s}$, shear stresses ranged from 73-81 MPa at $T \leq$
312 450°C , dropping to $\sim 60 \text{ MPa}$ at $T = 650^\circ\text{C}$ (weakening by $\sim 16\%$). In comparison, gouges
313 sheared at $V = 0.1 \mu\text{m/s}$ showed a larger reduction in shear stresses, going from 74 MPa at
314 450°C to $\sim 43 \text{ MPa}$ at 650°C (weakening by $\sim 42\%$). Overall, in our experiments, the
315 displacement-weakening and a notable reduction in steady-state shear stress occurred at $T \geq$
316 450°C and $V \leq 1 \mu\text{m/s}$. Once the weakening was triggered, lower sliding velocities led to
317 greater weakening over shorter critical displacements, ultimately resulting in lower steady-
318 state shear stresses.

319 3.2. Microstructures

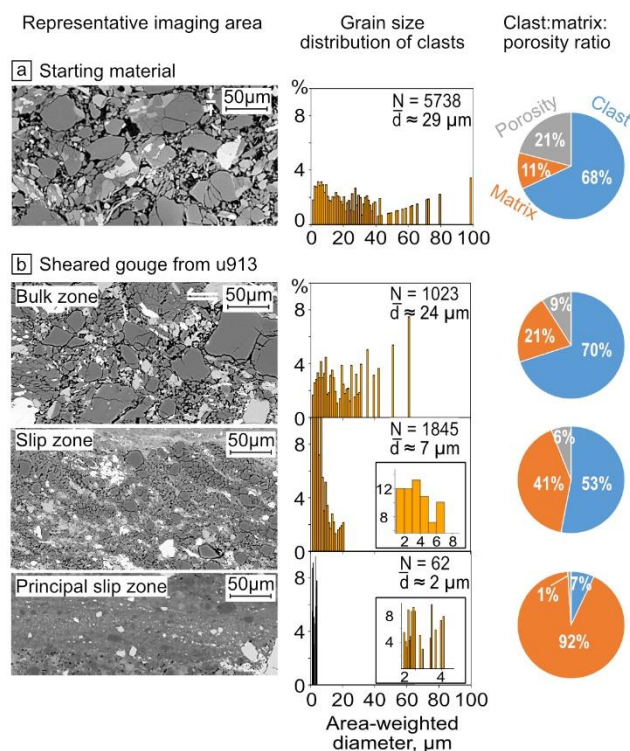
320 The mechanical data showed that considerable weakening occurred in granitoid gouge
321 as temperature increased and sliding velocity decreased. To understand the evolution of the
322 deformation processes during the transition from strong to weak gouges, we adopted a three-
323 step microstructural analysis. First, we used quantitative image analysis to systematically
324 categorize the strain localization consistently observed in the sheared gouges. Then, we
325 separately examined the effect of temperature and velocity on the microstructural evolution
326 of the whole gouge layer, by analyzing two experimental series with controlled
327 velocity/temperature conditions. Finally, we analyzed the grain-scale microstructural
328 evolution in two end-member cases: the strongest and the weakest gouges.

329 3.2.1. Strain localization in the deformed gouges

330 The microstructures of the sheared gouges were classified into three zones, based on
331 the degree of strain localization: the ‘bulk zone’, the ‘slip zone’ and the ‘principal slip zone’
332 (PSZ). The evaluation of localization was performed using quantitatively characterized
333 microstructural features, including the grain size distribution of clasts, and the
334 clast:matrix:porosity ratio (see definition in section 2.3). Notably, in zones with a higher
335 degree of strain localization, additional particles that were initially clasts were incorporated
336 into the fine-grained matrix. This led to a narrower grain size distribution of clasts and a
337 reduction in the mean size (\bar{d}). Consequently, this process led to a lower clast:matrix ratio,
338 and reduced porosity compared to less localized zones. Table S1 summarizes the width,
339 median, and mean particle size of localized zones of all sheared gouges.

340 To illustrate the varying degrees of strain localization, we show a quantitative
341 microstructural analysis of the sheared gouge from experiment u913 ($T = 650^\circ\text{C}$, $V = 1 \mu\text{m/s}$,
342 $D \approx 15 \text{ mm}$) and the starting material (compressed and held at $T = 650^\circ\text{C}$ for $\sim 4\text{h}$) (Figure 3).
343 The starting material showed homogeneously distributed compaction, characterized by
344 densely fractured, coarse-grained clasts, loosely consolidated among fine-grained clasts
345 (Figure 3a). Quantitative analysis revealed a clast size (d) that ranged between 1-98 μm with
346 a mean \bar{d} of $\sim 29 \mu\text{m}$, while the clast:matrix:porosity ratio was 68%:11%:21%. Owing to
347 shear deformation, sample u913 developed distinct strain localization and pervasive clast size
348 reduction, with a less localized bulk zone in the center, an intermediate localized slip zone,
349 and a highly localized PSZ towards the sample-piston interface (Figure 3b). The bulk zone
350 was characterized by a clast size d ranging from 1-61 μm with a mean $\bar{d} \approx 24 \mu\text{m}$ and a clast-

351 dominant texture (a clast:matrix:porosity ratio of 71%:29%:9%). In comparison, the slip zone
 352 had a narrower d ranging from 1-20 μm with a smaller \bar{d} of $\sim 7 \mu\text{m}$, and a higher proportion
 353 of matrix (a clast:matrix:porosity ratio of 53%:41%:6%). The PSZ showed the most intense
 354 clast size reduction and compaction, resulting in a clast size d ranging from 1-4 μm with a
 355 \bar{d} of $\sim 2 \mu\text{m}$, and a matrix-dominant texture (a clast:matrix:porosity ratio of 7%:92%:1%).
 356 High-magnification FEG-SEM images of PSZs indicated that the mean and median grain size
 357 of particles (clasts and matrix) were down to 0.6 μm and 1.2 μm , respectively. This
 358 quantitative analysis showed that sheared gouges developed three different microstructural
 359 domains, transitioning from the coarse-grained and porous bulk zone, comparable to the
 360 unsheared microstructure, to the medium-grained and less porous slip zone, and finally to the
 361 ultrafine-grained and dense PSZ. However, it should be noted that not all sheared gouges
 362 developed the aforementioned three microstructural domains, and many factors, including
 363 temperatures and sliding velocities, affected the level of strain localization. Section 3.2.2
 364 provides a detailed description of these factors.



365
 366 **Figure 3.** Quantitative microstructural analysis of (a) starting material ($T = 650^{\circ}\text{C}$, $V = 0$
 367 $\mu\text{m/s}$, $D = 0 \text{ mm}$) and (b) gouge from experiment u913 ($T = 650^{\circ}\text{C}$, $V = 1 \mu\text{m/s}$, $D \approx 15 \text{ mm}$),
 368 including three zones with varying degrees of deformation localization. Left column: the
 369 representative imaging areas cropped from the entire gouge layer. Central column: the grain
 370 size distribution of clasts from stitched BSE images. N = count numbers, \bar{d} = the mean

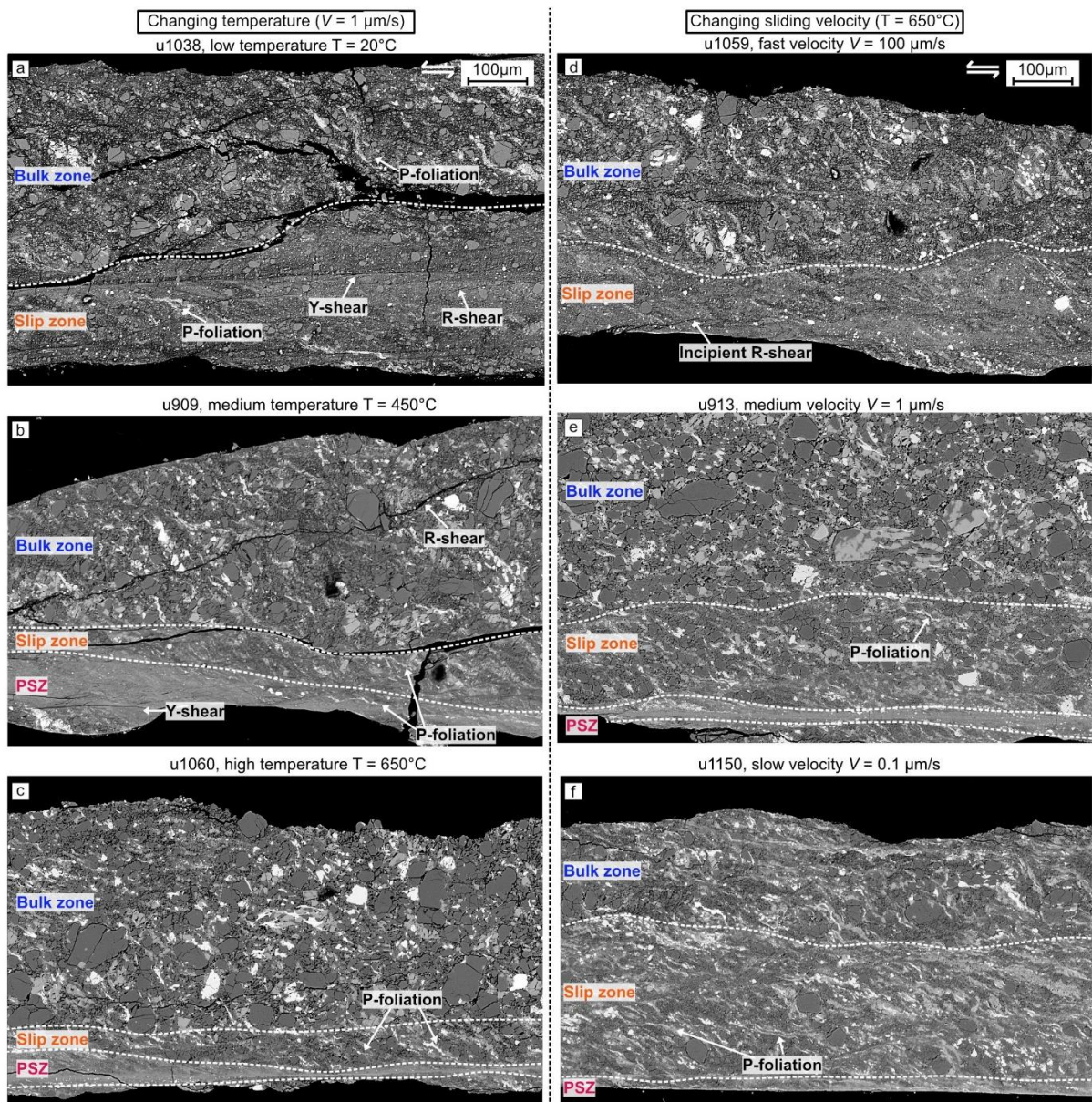
371 diameter. Right column: relative ratio of clasts-matrix-porosity, relative ratio equals to the
372 sum area of each phase divided by the entire imaging area.

373 3.2.2. Microstructural evolution of the whole gouge layer

374 We chose two experimental series to study the microstructural evolution
375 corresponding to the transition from high to low strength: one with increasing temperature of
376 $T = 20^{\circ}\text{C}$ - 450°C - 650°C and fixed velocity of $V = 1 \mu\text{m/s}$ (Figure 4a-4c), and the other with
377 decreasing velocity of $V = 100$ - 1 - $0.1 \mu\text{m/s}$ and fixed temperature of $T = 650^{\circ}\text{C}$ (Figure 4d-
378 4f).

379 In the first series of experiments, involving increasing temperature, all sheared
380 samples showed some level of strain localization (bulk, slip or principal slip zones), fracture
381 arrays (Y- and R-shears) and P-foliations (following terminology used by Logan et al., 1992;
382 Passchier & Trouw, 1996). P-foliations were defined by alternating layers of well-aligned
383 biotite and sigmoidal porphyroclasts of orthoclase (Figure 4f). The sample sheared at a low
384 temperature (20°C ; Figure 4a) showed a bulk zone and a slip zone, with no PSZ observed.
385 The width of the slip zone constituted up to $\sim 39\%$ of the total recovered gouge layer, with a
386 maximum width of $\sim 195 \mu\text{m}$ (Table S1). Note that the boundaries separating the designated
387 zones were not sharply defined, as transitions in the microstructural features between them
388 occurred gradually. Both bulk and slip zones were dissected by interface-parallel Y-shears
389 and inclined R-shears, which extend continuously up to $\sim 200 \mu\text{m}$ in length. P-foliations in the
390 slip zones were inclined at relatively low angles of $\sim 30^{\circ}$ to the shear plane, compared to $\sim 45^{\circ}$
391 in the bulk zones, indicating that larger shear strain was accommodated in the slip zones. For
392 the sample sheared at an intermediate temperature (450°C ; Figure 4b), a highly localized PSZ
393 evolved close to the sample-piston interface, with a width that constituted $\sim 10\%$ of the whole
394 gouge layer (a width of $\sim 83 \mu\text{m}$). The continuous intergranular fracture arrays remained
395 pervasive throughout the entire sample. Meanwhile, P-foliations in the slip zone and PSZ
396 became more abundant and exhibited lower angles to the shear plane compared to those
397 sheared at low temperatures in Figure 4a. As for the sample sheared at a high temperature
398 (650°C ; Figure 4c), deformation became even more localized, forming an extremely thin PSZ
399 with a width that constituted $\sim 5\%$ of the whole gouge layer (a width of $\sim 42 \mu\text{m}$). Continuous
400 intergranular fracture arrays in the slip zone and PSZ were replaced by closely spaced P-
401 foliations orientated subparallel at around 15° to the shear plane.

402 In comparison with the first series of experiments, the second series exhibited a
 403 similar change in microstructural features (Figure 4 right column). At fixed temperature and
 404 decreasing velocity, this series of samples showed more localized deformation occurring in
 405 PSZs, a reduction in the number of fracture arrays, and an increased intensity of P-foliations,
 406 with the predominant orientation aligning at around 15° to the shear plane. In general, all
 407 samples in the second series of experiments at high temperature ($T = 650^{\circ}\text{C}$) displayed only
 408 incipient fracture arrays, in contrast to the clear and distinct fracture arrays observed in the
 409 first series at lower temperatures $T \leq 450^{\circ}\text{C}$.



410
 411 **Figure 4.** Mosaics of backscatter images of the whole gouge layers, showing the effect of
 412 temperature (a-c, left column) and sliding velocity (d-f, right column). All samples have the
 413 same shear sense and scale bar, as shown in (a) and (d). Note that in the backscatter images,

414 quartz or albite appear as dark grey phases, orthoclase is light grey, biotite or epidote are
415 white phases.

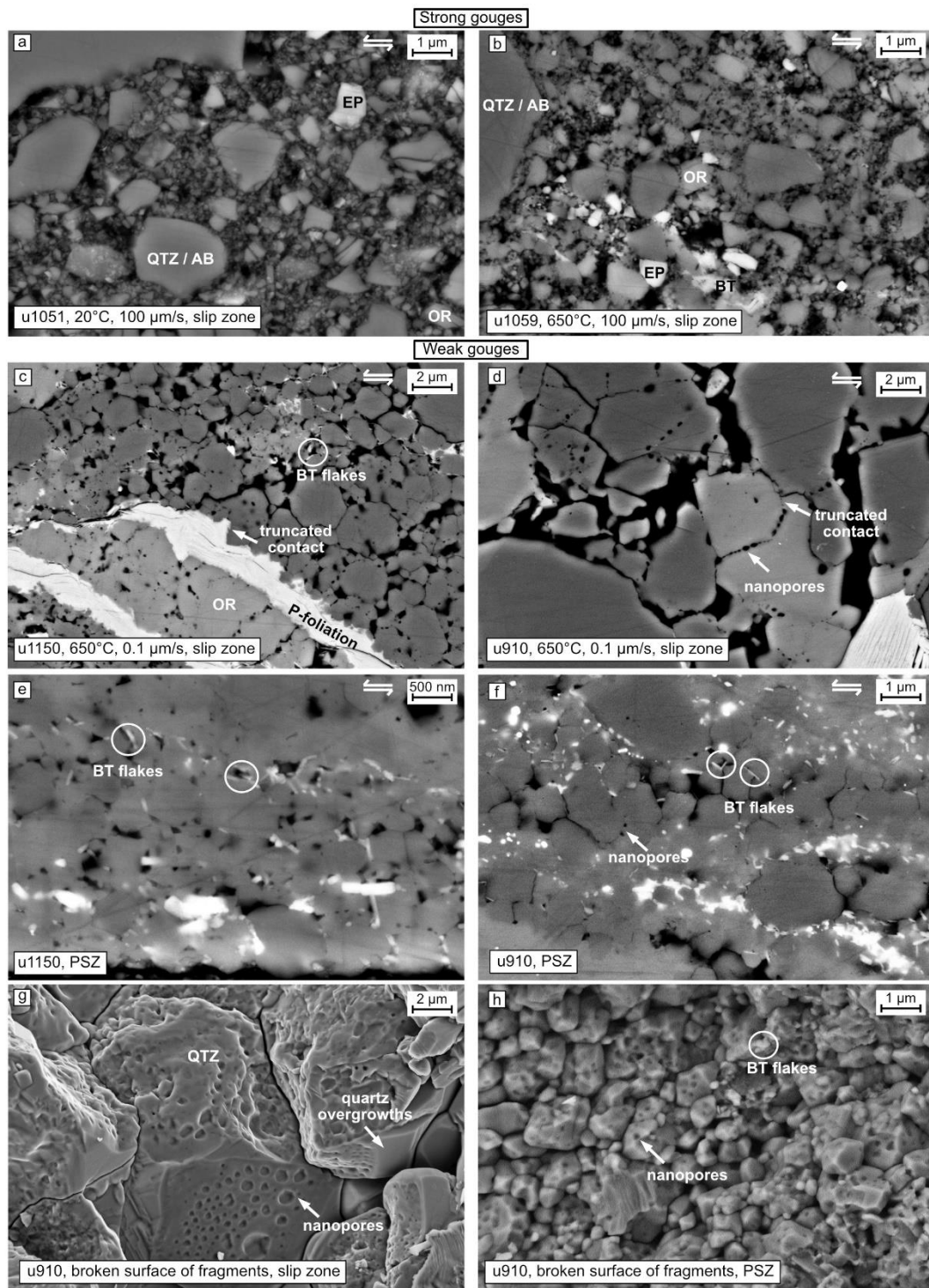
416 3.2.3. Grain-scale microstructural evolution

417 The observed ultrafine-grained and dense PSZs accommodated most of the total shear
418 strain. To gain an improved understanding of the deformation processes in these localized
419 zones, we conducted high-magnification FEG-SEM imaging on two extreme cases: the
420 strongest (u1051, u1059; Figure 5a-5b) and the weakest gouges (u1150, u910; Figure 5c-5f).

421 Samples tested in experiments u1051 ($\tau_{ss}=75$ MPa) and u1059 ($\tau_{ss}=82$ MPa)
422 exhibited the highest strengths. These samples underwent shearing at the highest velocity of
423 $V=100$ $\mu\text{m/s}$ and at $T=20^\circ\text{C}$ and 650°C , respectively. As shown in Figure 5a-5b, a detailed
424 examination of the grain-scale microstructures revealed that the slip zones formed in these
425 strong gouges exhibited clast-dominant gouge textures, where a large volume of fine-grained
426 matrix surrounded fractured angular clasts. The mean grain size of these slip zones was $\bar{d} \approx$
427 $3\text{-}6$ μm (Table S1).

428 Regarding the weak gouges recovered from experiments u1150 ($\tau_{ss}=49$ MPa) and
429 u910 ($\tau_{ss}=37$ MPa), these were subjected to the lowest velocity explored ($V=0.1$ $\mu\text{m/s}$) and
430 the highest temperature ($T=650^\circ\text{C}$). In comparison with the strong gouges, the slip zones
431 showed a marked increase in the proportion of clasts to matrix, with a larger fraction of
432 rounded clasts, plus well-developed P-foliations and truncated grain-to-grain contacts (Figure
433 5c-5d). Upon closer inspection, it became clear that sigmoidal porphyroclasts of orthoclase,
434 which defined P-foliation at a larger scale, were actually aggregates of many cataclastically
435 fragmented, equidimensional grains that had been smeared into a sigmoidal shape (Figure
436 5c). Truncated contacts and fluid inclusions were often found within these aggregates (Figure
437 5c). The PSZs contained sparsely distributed clasts embedded in a dense ultrafine-grained
438 matrix, consisting of well-mixed phases such as quartz and feldspar (Figure 5e-5f). Individual
439 grains were difficult to identify in backscatter electron imaging mode because of grain
440 aggregates being agglutinated together, resulting in low-relief grain boundaries. Semi-
441 quantitative analysis suggested the mean grain size of the PSZs was $\bar{d} \approx 0.6\text{-}1.1$ μm (Table
442 S1). In both slip zones and PSZs, we observed nanometer-sized pores, small biotite flakes
443 and quartz overgrowths on open pore walls (Figure 5g-5h). These nanopores were primarily
444 distributed along the grain contact surfaces (i.e. grain-to-grain boundaries), and sometimes
445 trapped inside grains as fluid inclusions. Their sizes ranged from a few nanometers in

446 diameter in the PSZs (Figure 5h), to larger diameters of up to 1 μm in the slip zones (Figure
 447 5g). Idiomorphic biotite flakes, which were remarkably small, measuring $\sim 30\text{ nm}$ in length
 448 and 10 nm in width often filled the nanopores. In these biotite flakes, we found no evidence
 449 for grain deformation, such as folding or kinking on the basal slip plane.



450
 451 **Figure 5.** Backscatter images showing the variation in grain-scale microstructures between
 452 strong (a-b) and weak gouges (c-h). Three-dimensional views of nanopores and regional

453 quartz overgrowths are displayed in (g-h). *QTZ* / *AB* quartz or albite; *OR* orthoclase; *EP*
 454 epidote; *BT* biotite.

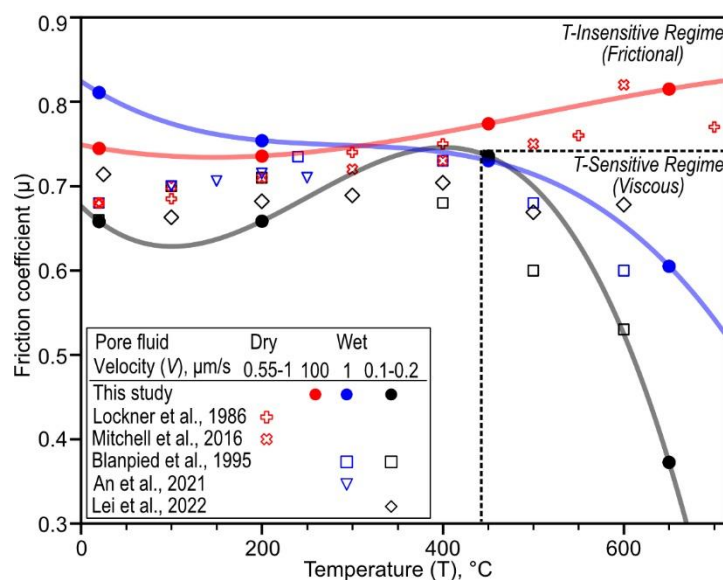
455 4 Discussion

456 4.1. Frictional and viscous regimes

457 To compare our mechanical data with previous studies conducted at different
 458 effective normal stresses, we convert the steady-state shear stresses (τ_{SS}) into apparent
 459 friction coefficients (μ_{SS}) according to the formula below:

$$460 \quad \mu_{SS} = \tau_{SS} / \sigma_n^{eff} \quad (2)$$

461 The effect of cohesion on friction coefficients is ignored, assuming this is negligible in
 462 powdered materials, in line with most previous works. The apparent friction coefficients
 463 obtained are shown against temperature in Figure 6, together with previously reported data.
 464 Table S2 summarizes the experimental conditions applied in the other studies and the range
 465 of measured friction coefficients. As shown in Figure 6, we classified the mechanical
 466 behavior of granitoid gouge in our study into two different regimes: the temperature-
 467 insensitive (frictional) regime and the temperature-sensitive (viscous) regime. This
 468 interpretation is consistent with the two regimes identified for westerly granite gouges
 469 (Blanpied et al., 1995), for pure quartz gouges (Chester & Higgs, 1992) and for calcite fault
 470 gouges (Verberne et al., 2015).



471 **Figure 6.** Comparison of steady-state friction coefficient for granitic gouges between our
 472 study and previous publications. Colorful shading and dashed lines are drawn as guides.
 473

474 Velocity refers to a range of displacement rates at which the friction coefficients were
475 selected. See Table S1 for experimental conditions applied in the previous studies.

476 In the temperature-insensitive regime, the apparent friction coefficients μ_{ss} were
477 generally high and relatively insensitive to temperature changes. In our study, this regime
478 includes samples deformed at $V = 100 \mu\text{m/s}$ and $T = 20\text{-}650^\circ\text{C}$, and those deformed at $V =$
479 $0.1\text{-}1 \mu\text{m/s}$ and $T < 450^\circ\text{C}$. Many studies on granitoid gouges have reported similar friction
480 coefficients (An et al., 2022; Blanpied et al., 1995; Kolawole et al., 2019; Lei et al., 2022a). It
481 is important to note that these studies covered a broader range of effective normal stresses
482 and pore fluid pressures in comparison to the conditions in our research (Table S2). This
483 consistency in friction coefficients across varying effective normal stress and pore fluid
484 pressure levels implies that the deformation mechanisms in this regime remain largely
485 unaffected by such changes. Consequently, this suggests that the deformation processes are
486 primarily frictional, similar to those observed in a wide range of frictionally deformed
487 materials, ranging from metals to a variety of rock types (Rabinowicz & Mutis, 1965; Scholz,
488 2019).

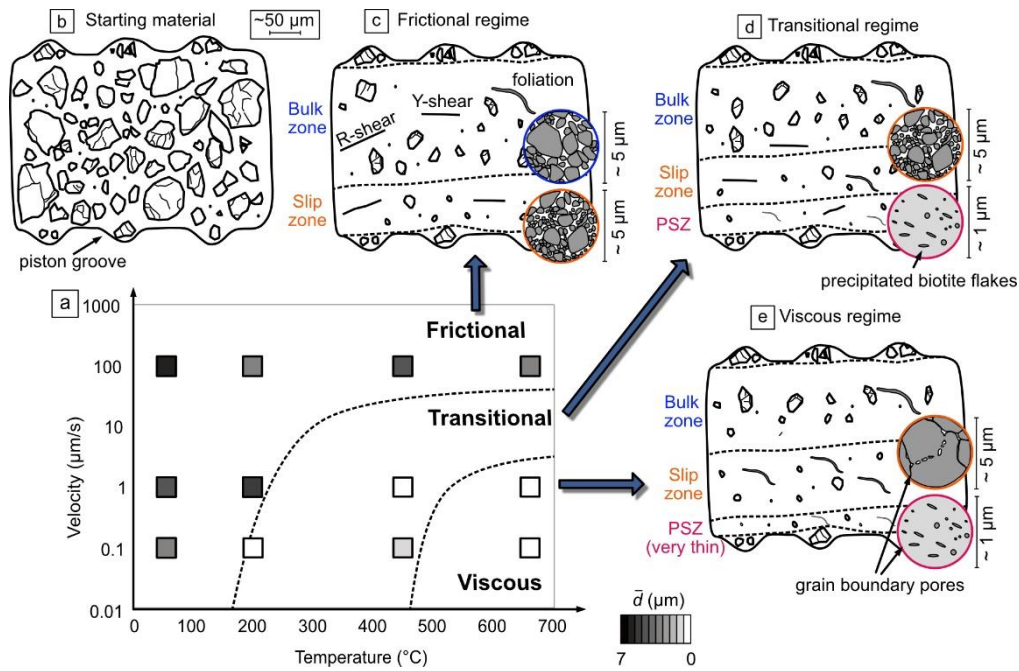
489 In the temperature-sensitive regime, μ_{ss} showed a notable decrease as temperature
490 increases. This regime includes samples deformed at $V = 0.1\text{-}1 \mu\text{m/s}$ and $T \geq 450^\circ\text{C}$. This
491 temperature-sensitive weakening behavior is most pronounced at a low sliding velocity of V
492 $= 0.1 \mu\text{m/s}$, where friction coefficients decreased from $\mu_{ss} = 0.74$ at 450°C to $\mu_{ss} = 0.37$ at
493 650°C , indicating also a rate-sensitivity in the viscous response. In addition, gouges sheared
494 under high pore fluid pressure showed a more pronounced weakening effect compared to
495 those with lower pore fluid pressure. For example, in our study, the apparent friction
496 coefficients of gouges sheared at $V = 0.1 \mu\text{m/s}$ and $P_f = 100 \text{MPa}$ decreased by $\Delta\mu_{ss} = 0.37$
497 from 450°C to 650°C . In contrast, experiments by Lei et al., 2022a showed that granitoid
498 gouges sheared at $V = 0.2 \mu\text{m/s}$ and $P_f = 30 \text{MPa}$ decreased by $\Delta\mu_{ss} = 0.03$ from 400°C to
499 600°C (Figure 6). This temperature-, rate- and pore pressure-sensitivity suggests that fluid-
500 assisted viscous processes predominantly govern deformation in this temperature-sensitive
501 regime.

502 In our study of granitoid gouges, the principal weakening effect is induced by
503 lowering the sliding velocity from $V = 100 \mu\text{m/s}$ to $V = 0.1$ or $1 \mu\text{m/s}$ and by increasing the
504 temperature from $T = 20^\circ\text{C}$ to at least $T \approx 400\text{-}450^\circ\text{C}$ (Figure 2d). The study of Blanpied et
505 al., 1995 has shown that at low velocities of $V \approx 1 \mu\text{m/s}$, the addition of pore fluids to dried

506 gouges significantly reduced the friction coefficients through fluid-assisted processes, from
507 $\mu_{SS} = 0.80$ to $\mu_{SS} = 0.58$ at 600°C. However, we observed that granitoid gouges subjected to
508 wet ($P_f = 100$ MPa) and fast shearing ($V = 100$ $\mu\text{m/s}$) showed high friction coefficients $\mu_{SS} =$
509 0.74-0.82, similar to $\mu_{SS} = 0.68$ -0.82 for gouges deformed at dry and low velocity conditions
510 by Lockner & Byerlee, 1986 and Mitchell et al., 2016 (where $P_f = 0$ MPa, $V = 0.55$ -1 $\mu\text{m/s}$).
511 Our experiments reveal that only the addition of pore fluids does not necessarily weaken the
512 gouge tested, but that fully water-saturated gouges with high pore fluid pressure can maintain
513 their ‘dry’ frictional strength when sheared at a high enough velocity. This may be attributed
514 to the dominance of frictional processes over time-dependent fluid-assisted processes at
515 sufficiently rapid shearing rates, where dissolution/precipitation kinetics are too slow to play
516 any role.

517 4.2. Deformation mechanisms

518 We use the schematic diagram in Figure 7 to comprehensively summarize the
519 microstructural evolution of our granitoid gouges from the frictional to the viscous regime as
520 a function of temperature and velocity. This diagram includes the microstructural changes at
521 the gouge scale, as well as those at the grain scale, and provides a basis for discussing the
522 operative deformation mechanisms. As shown in Figure 7b, the unsheared starting material is
523 characterized by coarse clasts and large porosity, without any indication of strain localization.
524 At low temperature or high velocity in the frictional regime, deformation is localized in a
525 thick slip zone (> 149 μm , $\bar{d} \approx 5$ μm) close to the sample-piston interface (Figure 7c). The
526 slip zones show clast-dominant texture, medium porosity and numerous fracture arrays. As
527 temperature increases and velocity decreases during the transitional regime, gouges exhibit a
528 higher degree of strain localization, resulting in a thin principal slip zone (PSZ) with mean
529 grain size $\bar{d} < 1$ μm forming adjacent to the broader, less localized slip zone (Figure 7d). The
530 PSZs show an ultrafine-grained and matrix-dominant texture with tiny biotite flakes filling
531 grain-grain boundaries, while the broader slip zones retain their clast-dominant texture but
532 with fewer fracture arrays and more closely spaced P-foliations. At the highest temperature
533 and lowest velocity in the viscous regime, deformation localizes even further into a still thin
534 PSZ (Figure 7e), whereas the slip zone shows a much smaller amount of fine-grained matrix,
535 less fractures arrays, but extensive boundary-subparallel P-foliations and nanopores at grain
536 contact surfaces.



537
 538 **Figure 7.** Schematic diagram summarizes the microstructural evolution from the frictional
 539 regime to the viscous regime as temperature increases, velocity decreases or grain size
 540 decreases. \bar{d} is the mean diameter of particles within the (principal) slip zone (see detailed
 541 data in Table S1).

542 4.2.1. Deformation mechanism in the frictional regime

543 Microstructural evidence indicates that the temperature-insensitive deformation
 544 mechanism governing granitoid gouge deformation in the frictional regime is cataclastic
 545 frictional granular flow. In this regime, our deformed gouges underwent substantial particle
 546 fragmentation, resulting in significant grain size reduction relative to the starting material
 547 (Figure 7b-7c). Angular grain boundaries, as shown in Figure 5b, suggest a process of grain
 548 crushing and fracturing, rather than the typical interlocking and discrete grain boundaries
 549 found in viscous processes like DPC (Kilian et al., 2011; Marti et al., 2017). Pervasive
 550 fracture arrays crosscut the entire gouge layers (Figure 4a), which is characteristic of
 551 frictionally deformed fault rocks from many experiments (An et al., 2022; Blanpied et al.,
 552 1995; Logan et al., 1992) and natural fault zones (Frederick M. Chester et al., 1993; Faulkner
 553 et al., 2010; Wehrens et al., 2016). Furthermore, deformation typically localized into slip
 554 zones near the sample-piston interface, adjacent to a bulk zone in the center (Figure 4a, 4d).
 555 Both slip and bulk zone underwent frictional deformation, indicated by the similar clast-
 556 dominant gouge texture found within these areas (see Figure 5a-5b). The slip zones
 557 accommodate more deformation than the bulk zones, owing to their smaller clast size, larger
 558 volume of fine-grained matrix, and foliations oriented more parallel to the shear planes

559 (Figure 4a). These microstructural observations indicate that materials adjacent to the
560 interface must have experienced a faster rate of deformation and correspondingly more
561 intense frictional deformation, compared to the central region. The observed high strength is
562 primarily determined by the actively deformed slip zones, where frictional resistance is
563 caused by grain rotations, localized sliding along angular grain boundaries and on fracture
564 arrays, i.e. by cataclastic frictional granular flow.

565 4.2.2. Deformation mechanisms in the viscous regime

566 Regarding gouges from the viscous regime, microstructural evidence points to the
567 simultaneous operation of DPC and cataclastic frictional granular flow. Specifically, gouges
568 within this regime exhibited few fracture arrays, more regular P-foliations defined by well-
569 aligned biotite and sigmoidal aggregates of fragmented orthoclase (Figure 4f). In nature, such
570 features are typical for viscously deformed mylonites that form at elevated
571 temperature/pressure conditions at depth (Passchier & Trouw, 1996; Smith et al., 2007;
572 Viegas et al., 2014). By analogy to previous studies (Barker et al., 1991; Spiers et al., 1990),
573 we infer for our experiments that the truncated and tight grain contacts indicate that
574 dissolution has occurred at these sites because of stress concentration (Figure 5c-5d).
575 Dissolved material is then transported and precipitated in dilatant, pore-rich domains under
576 reduced stress, as exemplified by the formation of overgrowths on existing grain surfaces
577 (quartz overgrowth in Figure 5g), or as precipitation along grain contacts (biotite flakes in
578 Figure 5e-5f). The newly grown biotite flakes are not only extremely small in size and
579 idiomorphic in shape, but also spatially clearly separated from the preexisting larger biotite
580 grains. These microstructural features suggest that the new grain formation involves a crucial
581 process of fluid-assisted mass transport exceeding the grain scale, which exclusively occurs
582 during DPC rather than dynamic recrystallization (Herwegh & Jenni, 2001; Lu & He, 2018;
583 Schwichtenberg et al., 2022).

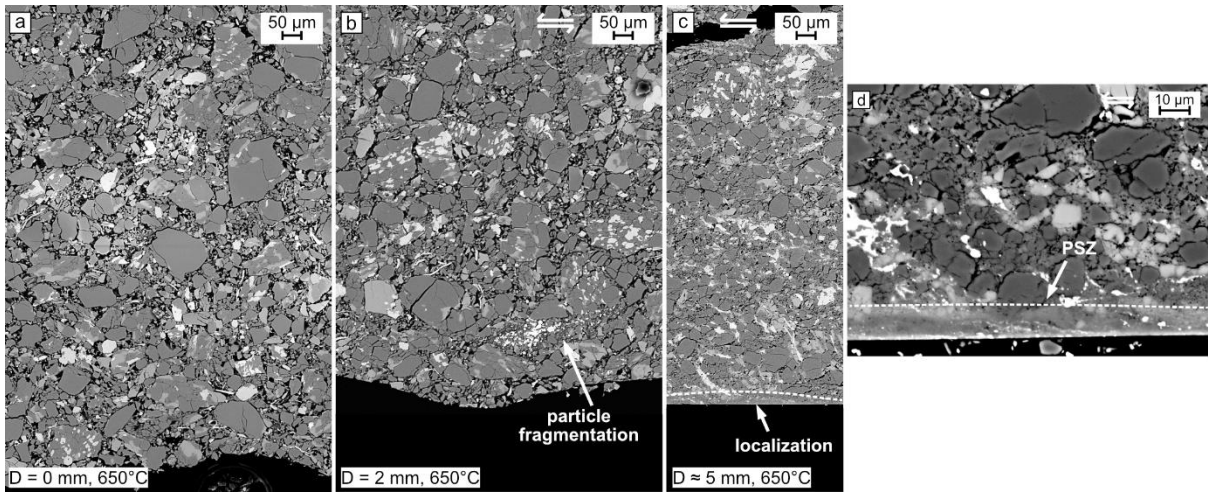
584 Additionally, many nanopores were located mostly along the grain contact surfaces
585 (Figure 5g), or within grains as fluid inclusions (Figure 5c-5d). These nanopores may either
586 have been trapped within crystals during rapid overgrowths (Craw & Norris, 1993), or
587 formed during preferential dissolution of crystallographic faces resulting in etch pits (Billia et
588 al., 2013). Another process worth considering in the context of pore formation/preservation is
589 creep cavitation during viscous grain boundary sliding (Fusseis et al., 2009; Gilgannon et al.,
590 2017, 2020; Kassner & Hayes, 2003; Ree, 1994), which might contribute to the nucleation of
591 these nanopores in the ultrafine-grained and dense domain (Figure 5h). While it remains

592 challenging to determine which of these mechanisms primarily governs the formation of
593 nanopores, the associated microstructures highlight the notably enhanced effect of viscous
594 processes relative to the frictional ones within this regime. The formation of potentially
595 interconnected dilatant openings provides the path for mass transportation, and creates space
596 for dissolved material to precipitate and develop.

597 The observed strength reduction in the viscous regime is closely associated with the
598 formation of the ultrafine-grained PSZ supporting a major role of a grain size sensitive creep
599 mechanism, namely DPC. DPC operates by facilitating small displacements between
600 intervening clasts through dissolving materials at the grain-to-grain contacts and then
601 transporting to regions with lower stress concentration (Bart Bos & Spiers, 2002; Niemeijer,
602 2018). Unlike the cataclastic frictional granular flow, the rate of DPC strongly increases with
603 decreasing grain size. This could be due to either a faster dissolution process, caused by a
604 higher reactive surface area (Anbeek, 1992), or quicker diffusive transport process due to
605 shorter transport distances at the grain scale (de Meer & Spiers, 1997; Xiangmin Zhang et al.,
606 2010). We infer that the extremely small grain size within the PSZs allows DPC to operate at
607 rates that are sufficiently rapid to accommodate the majority of sliding, and ultimately
608 resulting in a reduction in the gouge strength. Moreover, the development of biotite foliations
609 may also contribute to the reduction of gouge strength, e.g. through dislocation glide on the
610 basal plane (Lu & He, 2014; Okamoto et al., 2019; Shea & Kronenberg, 1992), or through
611 frictional slip on atomically flat basal planes (Aslin et al., 2019). Biotite, as a type of sheet
612 silicate, generally exhibits a higher frictional strength if deformation involves buckling,
613 bending or cleavage of grains (Niemeijer, 2018; Okamoto et al., 2019). Our microstructures
614 reveal that both primary and newly precipitated biotite flakes in PSZs are small enough to
615 inhibit buckling or further bending, thus reducing the apparent gouge strength (Figure 5e-5f,
616 supporting information Figure S4).

617 To understand the process of formation of the ultrafine-grained PSZ, we repeated the
618 experiment conducted at 650°C and 0.1 $\mu\text{m/s}$ but terminated it at displacements of ~ 2 mm
619 and ~ 5 mm. The sample sheared for ~ 2 mm displacement exhibited homogeneous
620 deformation similar to the starting material, with no indication of a PSZ. However, we
621 observed that some particles underwent substantial grain size reduction close to the boundary
622 (Figure 8a). Subsequent shearing for a larger displacement of ~ 5 mm resulted in the
623 development of a PSZ adjacent to the slip zone, characterized by microstructural features that
624 we have associated with viscous behavior involving DPC (Figure 8b-8c). This observation

625 suggests that a sufficient amount of displacement is necessary for frictional processes to
 626 reduce the grain size before activating grain-size-sensitive DPC within the PSZ. Once DPC is
 627 initiated, under considerably high temperature and slow velocity, the grain size may continue
 628 to decrease, through (subordinate) frictional processes or through dissolution and
 629 precipitation, resulting in additional strain localization or condensation of PSZ until a steady
 630 state condition is achieved.



631 **Figure 8.** Mosaics of backscatter images of the gouge layers sheared at $T = 650^{\circ}\text{C}$, $V = 0.1$
 632 $\mu\text{m/s}$ for (a) displacement of $D = 0$ mm, (b) $D = 2$ mm and (c) $D \approx 5$ mm. The effective
 633 normal stresses were 100 MPa, 80 MPa and 150 MPa, respectively. (d) The close-up view of
 634 strain localized area in (c).
 635

636 4.3. Rheology in the gradual transition from frictional to viscous regimes

637 In geologic materials and metallurgy, a standard power law is commonly used to
 638 characterize viscous or creep deformation, describing the dependency of strain rate on
 639 various factors such as differential stress, grain size and temperature. Such a constitutive flow
 640 law is generally expressed in the following general form (Gleason & Tullis, 1995; Twiss &
 641 Moores, 1992):

$$642 \quad \dot{\epsilon} = A\sigma^n d^{-m} f_{H_2O}^r \exp\left(-\frac{Q}{RT_K}\right) \quad (3)$$

643 Here, $\dot{\epsilon}$ represents axial or equivalent strain rate, A is the pre-exponential factor, σ^n is
 644 differential or deviatoric stress with exponent n , d^{-m} is the grain size with exponent m , $f_{H_2O}^r$
 645 is water fugacity with exponent r , Q is the activation energy, R is the gas constant, and T_K is
 646 temperature in Kelvin. Generally, rock flow strength shows a linear or non-linear relationship
 647 with strain rate in a viscously deforming system, with stress exponents (stress sensitivity of
 648 strain rate) ranging from $n = 1$ to $n = 4$ or 5 (Luan & Paterson, 1992; Rutter & Brodie, 2004a,

649 2004b). The specific n value serves as an indicator of the active creep mechanisms, such as
650 dislocation creep ($n = 3$ to 5 ; Weertman, 1978) and DPC ($n = 1$; Spiers et al., 1990). In
651 contrast, in a system undergoing purely frictional deformation, strain rate is extremely
652 sensitive to stress ($n \gg 5$), or conversely strength is only very weakly dependent on strain
653 rate (e.g. Chen et al., 2017).

654 To investigate in our experiments how temperature affects the transition from
655 cataclastic frictional granular flow (high n) to DPC (low n), we calculate the stress exponent
656 n using the following formulas:

$$657 \quad n = \frac{\partial \ln \dot{\epsilon}}{\partial \ln \sigma} \quad (4a)$$

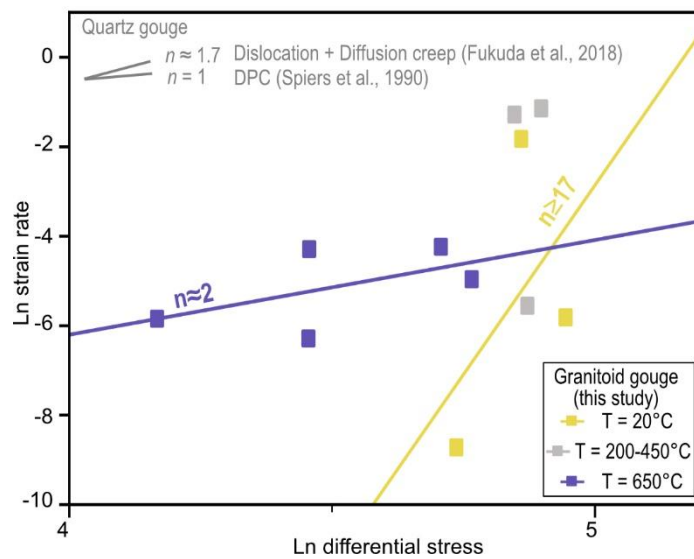
$$658 \quad \dot{\epsilon} = \frac{\dot{\gamma}}{\sqrt{3}} = \frac{V}{\sqrt{3}W} \quad (4b)$$

$$659 \quad \sigma = \sqrt{3}\tau_{ss} \quad (4c)$$

660 In these formulas, $\dot{\gamma}$ represents the shear strain rate, V is the applied sliding velocity, τ_{ss} is the
661 shear stress obtained in our study, W is the width of localized domains. The (equivalent)
662 differential stress (σ) and (equivalent) strain rate ($\dot{\epsilon}$) are calculated following the method
663 described by Verberne et al., 2017. Due to varying degrees of strain localization, we consider
664 W to be the width of slip zones measured in the experiments conducted at 20-450°C and the
665 width of the PSZs developed at 650°C (see detailed data in Table S3). In a log-log plot, the
666 resulting (equivalent) strain rates are plotted against (equivalent) differential stresses for
667 different temperatures ($T = 20, 200, 450, 650^\circ\text{C}$) (Figure 9). The slope (n) of the linear fits is
668 determined exclusively at temperatures of 20°C and 650°C, as these temperatures provide
669 enough data points to constrain the linear fits. Since quartz is generally considered to
670 represent the dominant weak phase in viscously deforming granitoid systems (Bürgmann &
671 Dresen, 2008; Kohlstedt et al., 1995), we also add the stress exponents obtained in quartz
672 deformation experiments as reported in literature.

673 As illustrated in Figure 9, though constrained by very few data, the n value for
674 granitoid gouges decreases as the temperature increases: from $n \geq 17$ at 20-450°C to $n \approx 2$ at
675 650°C. The high n values at low temperatures indicates that rock strength is almost
676 independent of strain rate, and cataclastic frictional granular flow governs the deformation.
677 At high temperature of 650°C, the low n value obtained for granitoid gouges closely aligns
678 with $n = 1.7$ for a mix of dislocation and diffusion creep in quartz (Fukuda et al., 2018), and

679 is close to $n = 1$ expected if DPC or DPC-accommodated granular flow becomes dominant.
 680 However, dislocation creep cannot account as a dominant mechanism in the case of our fine-
 681 grained polymineralic gouge aggregates due to the pinning effect of secondary phases (Kilian
 682 et al., 2011; Passchier & Trouw, 1996). Hence, the changes in n -values in Figure 9 suggest
 683 that the contributions of the end-member mechanisms change with temperature, from
 684 velocity-strengthening cataclastic frictional granular flow (Chen et al., 2017; Chen & Spiers,
 685 2016) to DPC-accommodated viscous granular flow becoming dominant, as temperatures
 686 exceed 450°C and as strain localizes into the ultra-fine grained PSZs.



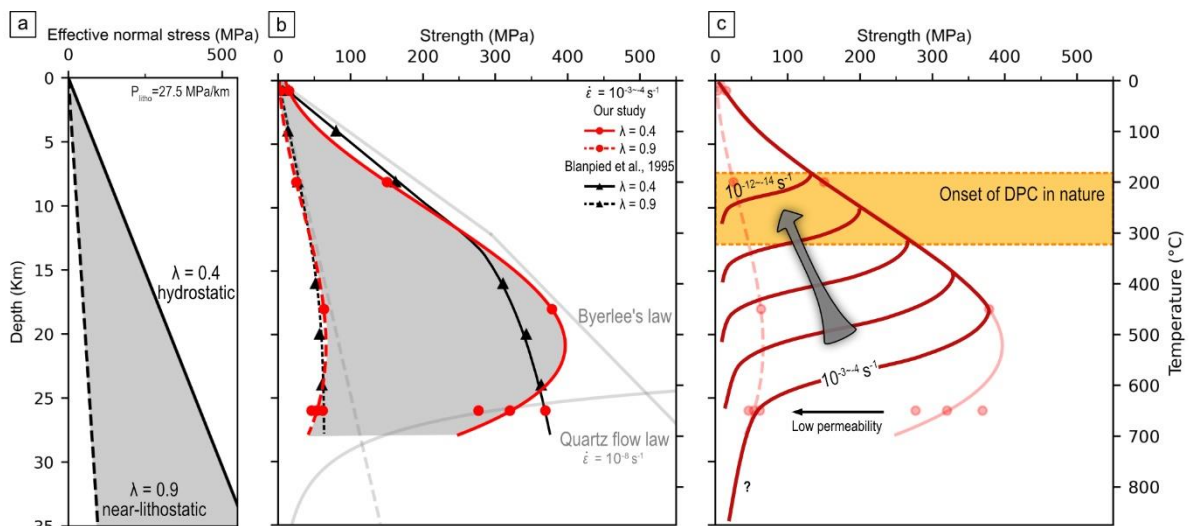
687
 688 **Figure 9.** Ln strain rate vs. Ln differential stress showing the effect of temperature on the
 689 stress exponent (n). Stress exponents of quartz gouges represent different creep mechanisms:
 690 $n \approx 1.7$ for a mixed dislocation and diffusion creep in quartz (Fukuda et al., 2018); $n = 1$
 691 predicted by conventional models for DPC (Spiers et al., 1990).

692 4.4. Implications for natural fault zones

693 It is important to note that our experimental findings can only be extrapolated to
 694 natural granitoid gouges under water saturated conditions and not for dry gouges. In Figure
 695 10, we extend the experimental strength data obtained in our experimental study to conditions
 696 representative of natural fault zones. This extension is established based on the following
 697 assumptions: (1) the strength refers to the differential stress needed for the initiation of
 698 sliding along a pre-existing fault plane under strike-slip kinematic conditions; (2) existence of
 699 a geothermal gradient of 25°C/km (e.g. estimates from the Aar Massif by Berger & Herwegh,
 700 2019; Musso Piantelli, 2023); (3) existence of a lithostatic pressure gradient of 27.5 MPa/km,
 701 following Blanpied et al., (1995). We examined two cases: the first case assumes an
 702 interconnected porosity and therefore the pore fluid pressure is hydrostatic ($\lambda =$ pore fluid

703 pressure/lithostatic pressure = 0.4); in the second case, substantial amounts of water are
 704 trapped and therefore isolated in pores meaning that the fluid pore pressure is close to the
 705 lithostatic pressure ($\lambda = 0.9$, close to a value of 1). Note that if we allow the state of stress to
 706 vary along changes in the kinematic framework (e.g. normal or thrust faulting), the amplitude
 707 of the strength envelope simply scales up/down, while the depth of the frictional-viscous
 708 transition remains relatively unaffected. Here, we focus on the strength envelope constructed
 709 based on aforementioned assumptions only.

710 For the hydrostatic and near-lithostatic fluid pressure conditions, the experimental
 711 (apparent) friction coefficients are extrapolated in the following way: first, the presumed
 712 geothermal gradient is used to extrapolate the experiment temperatures to the corresponding
 713 crustal depths. Then, the effective normal stress involves subtracting the pore fluid pressure
 714 from the normal stress expected at each depth (Figure 10a). The normal stress is obtained by
 715 multiplying the lithostatic pressure gradient with the depth calculated at the corresponding
 716 temperature, while the expected pore fluid pressure is determined as λ times the normal
 717 stress. Finally, the calculation of strengths involves multiplying the effective normal stress
 718 with the apparent friction coefficients (μ_{SS}) of those experiments sheared at a strain rate of 10^{-3}
 719 s^{-1} to $10^{-4} s^{-1}$ (sliding velocity $V = 0.1 \mu m/s$), as reported in Table 1, and converting them to
 720 differential stresses (strength) using formula (4c). The strength envelope is a curved best-fit
 721 line to the data points extrapolated from our experiments up to a temperature of $\sim 650^\circ C$,
 722 which corresponds to a depth of 26 km.



723 **Figure 10.** Extrapolation of experimental data for wet granitoid gouge to natural fault zones.
 724 The geothermal gradient is $25^\circ C/km$. In (a), the effective normal stress against depth assumed
 725 in two types of extrapolations: the hydrostatic pressure condition ($\lambda = 0.4$), and the near-
 726

727 lithostatic fluid pressure condition ($\lambda = 0.9$). (b) Plot of strength against depth, with
728 references to extrapolation of westerly granite gouges (Blanpied et al., 1995, recalculated
729 according to the assumptions in this study), Byerlee's law (J. Byerlee, 1978) and the quartz
730 flow law (Fukuda et al., 2018). $\dot{\epsilon}$ = (equivalent) strain rate. The curved strength envelope is
731 the best-fit line to the data points. (c) Conceptually extrapolated strength to slow strain rates
732 of $10^{-12}\sim 10^{-14} \text{ s}^{-1}$ typical in natural fault zones. Yellow rectangle indicates the onset temperature
733 of dissolution-precipitation creep in nature.

734 Our extrapolation in Figure 10b shows that the predicted strengths are generally much
735 lower in the case of near-lithostatic fluid pressures, with a peak value of ~ 60 MPa, compared
736 to a peak value of ~ 360 MPa in the hydrostatic pressure conditions. For both cases, the
737 calculated strengths of granitoid gouges increase nearly linearly with depth, down up to ~ 18
738 km, which aligns well with the previous extrapolation of sheared granitic gouges from
739 Blanpied et al., 1995 and Byerlee's law. However, a significant deviation occurs at greater
740 depths, where calculated strengths from our study show a substantial decrease at a depth of
741 >20 km, particularly in the hydrostatic conditions. This difference in extrapolated strengths
742 may be attributed to variations in the total displacement applied in these two studies. In our
743 study, gouges that underwent displacement-weakening reached a (near) steady state low
744 strength after sliding for a minimum of ~ 3 mm displacement (Figure 2c). In contrast,
745 Blanpied et al.'s 1995 study sheared gouges at a similar slow strain rate but only for <1 mm
746 displacement, preventing steady state to be reached. Our results emphasize the importance of
747 not only relatively high temperature and slow strain rates, but also of sufficient displacement
748 for grain size reduction to activate DPC and to activate further weakening (see section 4.2.2).

749 These findings from our study have important consequences for the extrapolation of
750 our experimental results to natural conditions with commonly much slower strain rates
751 (except for seismic and slow slip cycles), and much lower permeability at middle-lower
752 crustal levels predicted by crustal-scale models (Ingebritsen & Manning, 1999). Under low
753 temperature and shallow crustal conditions, granitoid fault gouges are typically non-cohesive,
754 porous and do not display substantial fault healing by cementation processes (exceptions are
755 hydrothermally active fault zones, e.g. see Berger & Herwegh, 2019, 2022; Niwa et al.,
756 2016). In this case, pores are interconnected, therefore the pore fluid pressure is hydrostatic.
757 Under high temperature and deeper crustal conditions, elevated pore fluids successively form
758 because fluids become trapped along grain boundary pores or along transgranular cracks and
759 cementation (fault healing; Tenthorey et al., 2003). Consequently, interconnectivity of pore

760 spaces decreases and so does the permeability. In our case, the near-lithostatic pressure
761 condition is valid for natural gouges at the same rates as in the experiments at $T \geq 450^\circ\text{C}$.
762 This is consistent with abundant nanopore inclusions formed within dense PSZs due to DPC-
763 accommodated viscous granular flow (see section 3.2.3). With these considerations, as shown
764 in Figure 10c, the strength envelope of natural fault zones are a combination of two end
765 member cases studied: a hydrostatic case at $T < 450^\circ\text{C}$ and a near-lithostatic fluid pressure
766 case in the range of $T = 450^\circ\text{C}$ - 650°C .

767 Furthermore, the laboratory observed DPC-induced weakening effect is expected to
768 occur at all P/T conditions where natural records of synkinematic dissolution-precipitation
769 processes are found in granitoid gouges. Newly precipitated mica (Berger et al., 2017),
770 stylolites (Groshong, Jr., 1988) and fluid inclusions (Harrison & Onasch, 2000) in granitoid
771 rocks were found in the temperature range of 180°C - 320°C , which corresponds to
772 anchizonal, in combination with the variations in sliding velocities and grain sizes under
773 natural deformation conditions, are important parameters which can explain the wide depth
774 range (7-20 km) of the viscous-frictional transition inferred for the granitoid continental
775 crust.

776 **5 Conclusions**

777 We performed sliding experiments on granitoid gouges at a broad range of sliding
778 velocities ($V = 0.1, 1, 100 \mu\text{m/s}$) and temperatures ($T = 20, 200, 450, 650^\circ\text{C}$), over a large
779 displacement of ~ 15 mm, and at an effective normal stress and pore fluid pressure of 100
780 MPa, respectively. Microstructures of compacted-only and sheared samples were
781 quantitatively analyzed. The following conclusions can be drawn:

782 1. The strength of granitoid gouge was reduced from $\tau_{ss} \approx 75$ MPa at $T = 20^\circ\text{C}$ and V
783 $= 100 \mu\text{m/s}$, to $\tau_{ss} \approx 37$ MPa at $T = 650^\circ\text{C}$ and $V = 0.1 \mu\text{m/s}$.

784 2. As the gouge weakened, strain localized into an ultrafine-grained and dense
785 principal slip zone (PSZ), where nanopores were located along grain contact surfaces and
786 contained biotite-quartz-feldspar precipitates. This evolution in microstructures indicates a
787 transition in deformation mechanisms from cataclastic frictional granular flow to dissolution-
788 precipitation creep (DPC) accommodated viscous granular flow.

789 3. The frictional-viscous transition occurred at $T \geq 450^\circ\text{C}$, $V \leq 1 \mu\text{m/s}$, and/or for a
790 median grain size $< \sim 1 \mu\text{m}$ under the hydrothermal conditions tested in our study.

791 4. Prior to the formation of a PSZ and associated gouge weakening, gouges sheared at
792 a short displacement of $\sim 2 \mu\text{m}$ underwent substantial grain size reduction close to the sample
793 boundary, suggesting that a sufficient additional displacement is necessary (i.e. a
794 displacement and grain size threshold must be overcome) to activate DPC.

795 6. Though poorly constrained by only limited data, the average stress exponent (n) at
796 the deformation temperature of 20-450°C was ≥ 17 , and at 650°C was ~ 2 , suggesting an
797 increased contribution of DPC at high temperature.

798 7. Extrapolations of experimental data to construct crustal strength suggest that the
799 frictional-viscous transition may be triggered at temperatures of 180-320°C (or depth of 7-20
800 km depending on the geothermal gradient), at slow natural strain rates and in ultrafine-
801 grained fault gouges, due to activation of DPC.

802 **Acknowledgments**

803 We thank Thony van der Gon Netscher, Gerard Kuijpers, and Floris van Oort for technical
804 supports of the ring shear apparatus, Beatrice Frey for support in the FEG-SEM works, and
805 Frank Emanuel Gfeller for support in the XRD works. This study is funded by the Swiss
806 National Science Foundation (SNSF) grant number 192124.

807 **Open Research**

808 Experimental data are freely available from the BORIS data repository:
809 <https://boris.unibe.ch/id/eprint/191713>

810 **References**

- 811 An, M., Zhang, F., Min, K., Elsworth, D., He, C., & Zhao, L. (2022). Frictional Stability of
812 Metamorphic Epidote in Granitoid Faults Under Hydrothermal Conditions and
813 Implications for Injection-Induced Seismicity. *Journal of Geophysical Research:*
814 *Solid Earth*, 127(3), e2021JB023136. <https://doi.org/10.1029/2021JB023136>
- 815 Anbeek, C. (1992). The dependence of dissolution rates on grain size for some fresh and
816 weathered feldspars. *Geochimica et Cosmochimica Acta*, 56(11), 3957–3970.
817 [https://doi.org/10.1016/0016-7037\(92\)90009-8](https://doi.org/10.1016/0016-7037(92)90009-8)

818 Aslin, J., Mariani, E., Dawson, K., & Barsoum, M. W. (2019). Rippllocations provide a new
819 mechanism for the deformation of phyllosilicates in the lithosphere. *Nature*
820 *Communications*, 10(1), 686. <https://doi.org/10.1038/s41467-019-08587-2>

821 Barbarin, B. (1999). A review of the relationships between granitoid types, their origins and
822 their geodynamic environments. *Lithos*, 46(3), 605–626.
823 [https://doi.org/10.1016/S0024-4937\(98\)00085-1](https://doi.org/10.1016/S0024-4937(98)00085-1)

824 Barker, C. E., Burruss, R. C., Kopp, O. C., Machel, H. G., Marshall, D. J., Wright, P., &
825 Colbum, H. Y. (1991). *Luminescence Microscopy and Spectroscopy Qualitative and*
826 *Quantitative Applications*. SEPM Society for Sedimentary Geology.
827 <https://doi.org/10.2110/scn.91.25>

828 Baumberger, R., Herwegh, M., & Kissling, E. (2022). Remote Sensing and Field Data Based
829 Structural 3D Modelling (Haslital, Switzerland) in Combination with Uncertainty
830 Estimation and Verification by Underground Data. In *3D Digital Geological Models*
831 (pp. 159–197). John Wiley & Sons, Ltd. <https://doi.org/10.1002/9781119313922.ch10>

832 Behnsen, J., & Faulkner, D. R. (2011). Water and argon permeability of phyllosilicate
833 powders under medium to high pressure. *Journal of Geophysical Research: Solid*
834 *Earth*, 116(B12). <https://doi.org/10.1029/2011JB008600>

835 Berger, A., & Herwegh, M. (2019). Cockade structures as a paleo-earthquake proxy in upper
836 crustal hydrothermal systems. *Scientific Reports*, 9(1), 9209.
837 <https://doi.org/10.1038/s41598-019-45488-2>

838 Berger, A., & Herwegh, M. (2022). Grain-size-reducing- and mass-gaining processes in
839 different hydrothermal fault rocks. *Geological Magazine*, 159(11–12), 2219–2237.
840 <https://doi.org/10.1017/S0016756822000218>

- 841 Berger, A., Herwegh, M., Schwarz, J.-O., & Putlitz, B. (2011). Quantitative analysis of
842 crystal/grain sizes and their distributions in 2D and 3D. *Journal of Structural Geology*,
843 33(12), 1751–1763. <https://doi.org/10.1016/j.jsg.2011.07.002>
- 844 Berger, A., Wehrens, P., Lanari, P., Zwingmann, H., & Herwegh, M. (2017). Microstructures,
845 mineral chemistry and geochronology of white micas along a retrograde evolution:
846 An example from the Aar massif (Central Alps, Switzerland). *Tectonophysics*, 721,
847 179–195. <https://doi.org/10.1016/j.tecto.2017.09.019>
- 848 Billia, M. A., Timms, N. E., Toy, V. G., Hart, R. D., & Prior, D. J. (2013). Grain boundary
849 dissolution porosity in quartzofeldspathic ultramylonites: Implications for
850 permeability enhancement and weakening of mid-crustal shear zones. *Journal of*
851 *Structural Geology*, 53, 2–14. <https://doi.org/10.1016/j.jsg.2013.05.004>
- 852 Blanpied, M. L., Lockner, D. A., & Byerlee, J. D. (1995). Frictional slip of granite at
853 hydrothermal conditions. *Journal of Geophysical Research: Solid Earth*, 100(B7),
854 13045–13064. <https://doi.org/10.1029/95JB00862>
- 855 Bos, B., & Spiers, C. J. (2001). Experimental investigation into the microstructural and
856 mechanical evolution of phyllosilicate-bearing fault rock under conditions favouring
857 pressure solution. *Journal of Structural Geology*, 23(8), 1187–1202.
858 [https://doi.org/10.1016/S0191-8141\(00\)00184-X](https://doi.org/10.1016/S0191-8141(00)00184-X)
- 859 Bos, Bart, & Spiers, C. J. (2002). Frictional-viscous flow of phyllosilicate-bearing fault rock:
860 Microphysical model and implications for crustal strength profiles. *Journal of*
861 *Geophysical Research: Solid Earth*, 107(B2), ECV 1-1-ECV 1-13.
862 <https://doi.org/10.1029/2001JB000301>
- 863 Bürgmann, R., & Dresen, G. (2008). Rheology of the Lower Crust and Upper Mantle:
864 Evidence from Rock Mechanics, Geodesy, and Field Observations. *Annual Review of*

865 *Earth and Planetary Sciences*, 36(1), 531–567.
866 <https://doi.org/10.1146/annurev.earth.36.031207.124326>

867 Burov, E. B. (2011). Rheology and strength of the lithosphere. *Marine and Petroleum*
868 *Geology*, 28(8), 1402–1443. <https://doi.org/10.1016/j.marpetgeo.2011.05.008>

869 Byerlee, J. (1978). Friction of Rocks. In J. D. Byerlee & M. Wyss (Eds.), *Rock Friction and*
870 *Earthquake Prediction* (pp. 615–626). Basel: Birkhäuser. [https://doi.org/10.1007/978-](https://doi.org/10.1007/978-3-0348-7182-2_4)
871 [3-0348-7182-2_4](https://doi.org/10.1007/978-3-0348-7182-2_4)

872 Chen, J., & Spiers, C. J. (2016). Rate and state frictional and healing behavior of carbonate
873 fault gouge explained using microphysical model: Microphysical Model for Friction.
874 *Journal of Geophysical Research: Solid Earth*, 121(12), 8642–8665.
875 <https://doi.org/10.1002/2016JB013470>

876 Chen, J., Niemeijer, A. R., & Spiers, C. J. (2017). Microphysically Derived Expressions for
877 Rate-and-State Friction Parameters, a , b , and D_c : Microphysically Derived RSF
878 Parameters. *Journal of Geophysical Research: Solid Earth*, 122(12), 9627–9657.
879 <https://doi.org/10.1002/2017JB014226>

880 Chester, F. M., & Higgs, N. G. (1992). Multimechanism friction constitutive model for
881 ultrafine quartz gouge at hypocentral conditions. *Journal of Geophysical Research:*
882 *Solid Earth*, 97(B2), 1859–1870. <https://doi.org/10.1029/91JB02349>

883 Chester, Frederick M., Evans, J. P., & Biegel, R. L. (1993). Internal structure and weakening
884 mechanisms of the San Andreas Fault. *Journal of Geophysical Research: Solid Earth*,
885 98(B1), 771–786. <https://doi.org/10.1029/92JB01866>

886 Craw, D., & Norris, R. J. (1993). Grain boundary migration of water and carbon dioxide
887 during uplift of garnet-zone Alpine Schist, New Zealand. *Journal of Metamorphic*
888 *Geology*, 11(3), 371–378. <https://doi.org/10.1111/j.1525-1314.1993.tb00154.x>

889 Evans, B., Fredrich, J. T., & Wong, T.-F. (1990). The Brittle-Ductile Transition in Rocks:
890 Recent Experimental and Theoretical Progress. In *The Brittle-Ductile Transition in*
891 *Rocks* (pp. 1–20). American Geophysical Union (AGU).
892 <https://doi.org/10.1029/GM056p0001>

893 Faulkner, D. R., Jackson, C. A. L., Lunn, R. J., Schlische, R. W., Shipton, Z. K., Wibberley,
894 C. A. J., & Withjack, M. O. (2010). A review of recent developments concerning the
895 structure, mechanics and fluid flow properties of fault zones. *Journal of Structural*
896 *Geology*, 32(11), 1557–1575. <https://doi.org/10.1016/j.jsg.2010.06.009>

897 Fukuda, J., Holyoke, C. W., & Kronenberg, A. K. (2018). Deformation of Fine-Grained
898 Quartz Aggregates by Mixed Diffusion and Dislocation Creep. *Journal of*
899 *Geophysical Research: Solid Earth*, 123(6), 4676–4696.
900 <https://doi.org/10.1029/2017JB015133>

901 Fusseis, F., Regenauer-Lieb, K., Liu, J., Hough, R. M., & De Carlo, F. (2009). Creep
902 cavitation can establish a dynamic granular fluid pump in ductile shear zones. *Nature*,
903 459(7249), 974–977. <https://doi.org/10.1038/nature08051>

904 Giese, J., Seward, D., Stuart, F. M., Wüthrich, E., Gnos, E., Kurz, D., et al. (2010).
905 Electrodynamic Disaggregation: Does it Affect Apatite Fission-Track and (U-Th)/He
906 Analyses? *Geostandards and Geoanalytical Research*, 34(1), 39–48.
907 <https://doi.org/10.1111/j.1751-908X.2009.00013.x>

908 Gilgannon, J., Fusseis, F., Menegon, L., Regenauer-Lieb, K., & Buckman, J. (2017).
909 Hierarchical creep cavity formation in an ultramylonite and implications for phase
910 mixing. *Solid Earth*, 8(6), 1193–1209. <https://doi.org/10.5194/se-8-1193-2017>

911 Gilgannon, J., Poulet, T., Berger, A., Barnhoorn, A., & Herwegh, M. (2020). Dynamic
912 Recrystallization Can Produce Porosity in Shear Zones. *Geophysical Research Letters*,
913 47(7), e2019GL086172. <https://doi.org/10.1029/2019GL086172>

914 Gleason, G. C., & Tullis, J. (1995). A flow law for dislocation creep of quartz aggregates
915 determined with the molten salt cell. *Tectonophysics*, 247(1), 1–23.
916 [https://doi.org/10.1016/0040-1951\(95\)00011-B](https://doi.org/10.1016/0040-1951(95)00011-B)

917 Goetze, C., & Evans, B. (1979). Stress and temperature in the bending lithosphere as
918 constrained by experimental rock mechanics. *Geophysical Journal International*,
919 59(3), 463–478. <https://doi.org/10.1111/j.1365-246X.1979.tb02567.x>

920 Gratier, J.-P., Dysthe, D. K., & Renard, F. (2013). The Role of Pressure Solution Creep in the
921 Ductility of the Earth's Upper Crust. In *Advances in Geophysics* (Vol. 54, pp. 47–
922 179). Elsevier. <https://doi.org/10.1016/B978-0-12-380940-7.00002-0>

923 Gratier, J.-P., Menegon, L., & Renard, F. (2023). Pressure Solution Grain Boundary Sliding
924 as a Large Strain Mechanism of Superplastic Flow in the Upper Crust. *Journal of*
925 *Geophysical Research: Solid Earth*, 128(4), e2022JB026019.
926 <https://doi.org/10.1029/2022JB026019>

927 Griggs, D. (1967). Hydrolytic Weakening of Quartz and Other Silicates*. *Geophysical*
928 *Journal of the Royal Astronomical Society*, 14(1–4), 19–31.
929 <https://doi.org/10.1111/j.1365-246X.1967.tb06218.x>

930 Groshong, Jr., R. H. (1988). Low-temperature deformation mechanisms and their
931 interpretation. *Geological Society of America Bulletin*, 100(9), 1329–1360.
932 [https://doi.org/10.1130/0016-7606\(1988\)100<1329:LTDMAT>2.3.CO;2](https://doi.org/10.1130/0016-7606(1988)100<1329:LTDMAT>2.3.CO;2)

933 Harrison, M. J., & Onasch, C. M. (2000). Quantitative assessment of low-temperature
934 deformation mechanisms in a folded quartz arenite, Valley and Ridge Province, West
935 Virginia. *Tectonophysics*, 317(1–2), 73–91. [https://doi.org/10.1016/S0040-](https://doi.org/10.1016/S0040-1951(99)00271-1)
936 [1951\(99\)00271-1](https://doi.org/10.1016/S0040-1951(99)00271-1)

937 den Hartog, S. A. M., Niemeijer, A. R., & Spiers, C. J. (2012). New constraints on
938 megathrust slip stability under subduction zone P–T conditions. *Earth and Planetary
939 Science Letters*, 353–354, 240–252. <https://doi.org/10.1016/j.epsl.2012.08.022>

940 Herwegh, M., & Jenni, A. (2001). Granular flow in polymineralic rocks bearing sheet
941 silicates: new evidence from natural examples.

942 Hickman, S., Sibson, R., & Bruhn, R. (1995). Introduction to Special Section: Mechanical
943 Involvement of Fluids in Faulting. *Journal of Geophysical Research: Solid Earth*,
944 100(B7), 12831–12840. <https://doi.org/10.1029/95JB01121>

945 Hirth, G., & Tullis, J. (1992). Dislocation creep regimes in quartz aggregates. *Journal of
946 Structural Geology*, 14(2), 145–159. [https://doi.org/10.1016/0191-8141\(92\)90053-Y](https://doi.org/10.1016/0191-8141(92)90053-Y)

947 Hirth, G., & Tullis, J. (1994). The brittle-plastic transition in experimentally deformed quartz
948 aggregates. *Journal of Geophysical Research: Solid Earth*, 99(B6), 11731–11747.
949 <https://doi.org/10.1029/93JB02873>

950 Ingebritsen, S. E., & Manning, C. E. (1999). Geological implications of a permeability-depth
951 curve for the continental crust. *Geology*, 27(12), 1107. [https://doi.org/10.1130/0091-
952 7613\(1999\)027<1107:GIOAPD>2.3.CO;2](https://doi.org/10.1130/0091-7613(1999)027<1107:GIOAPD>2.3.CO;2)

953 Johannes, W. (1984). Beginning of melting in the granite system Qz-Or-Ab-An-H₂O.
954 *Contributions to Mineralogy and Petrology*, 86(3), 264–273.
955 <https://doi.org/10.1007/BF00373672>

956 Kassner, M. E., & Hayes, T. A. (2003). Creep cavitation in metals. *International Journal of
957 Plasticity*, 19(10), 1715–1748. [https://doi.org/10.1016/S0749-6419\(02\)00111-0](https://doi.org/10.1016/S0749-6419(02)00111-0)

958 Kilian, R., Heilbronner, R., & Stünitz, H. (2011). Quartz grain size reduction in a granitoid
959 rock and the transition from dislocation to diffusion creep. *Journal of Structural
960 Geology*, 33(8), 1265–1284. <https://doi.org/10.1016/j.jsg.2011.05.004>

961 Kirkpatrick, J. D., Fagereng, Å., & Shelly, D. R. (2021). Geological constraints on the
962 mechanisms of slow earthquakes. *Nature Reviews Earth & Environment*, 2(4), 285–
963 301. <https://doi.org/10.1038/s43017-021-00148-w>

964 Kohlstedt, D. L., Evans, B., & Mackwell, S. J. (1995). Strength of the lithosphere:
965 Constraints imposed by laboratory experiments. *Journal of Geophysical Research:*
966 *Solid Earth*, 100(B9), 17587–17602. <https://doi.org/10.1029/95JB01460>

967 Kolawole, F., Johnston, C. S., Morgan, C. B., Chang, J. C., Marfurt, K. J., Lockner, D. A., et
968 al. (2019). The susceptibility of Oklahoma’s basement to seismic reactivation. *Nature*
969 *Geoscience*, 12(10), 839–844. <https://doi.org/10.1038/s41561-019-0440-5>

970 Labuz, J. F., & Zang, A. (2012). Mohr–Coulomb Failure Criterion. *Rock Mechanics and*
971 *Rock Engineering*, 45(6), 975–979. <https://doi.org/10.1007/s00603-012-0281-7>

972 Lamadrid, H. M., Lamb, W. M., Santosh, M., & Bodnar, R. J. (2014). Raman spectroscopic
973 characterization of H₂O in CO₂-rich fluid inclusions in granulite facies metamorphic
974 rocks. *Gondwana Research*, 26(1), 301–310. <https://doi.org/10.1016/j.gr.2013.07.003>

975 Lei, H., Zhou, Y., Yao, W., Ma, X., He, C., Dang, J., et al. (2022). Earthquake nucleation
976 conditions of Anninghe Fault constrains from frictional experiments on natural granite
977 gouge. *Chinese Journal of Geophysics*, 65(3), 978–991.
978 <https://doi.org/10.6038/cjg2022P0248>

979 Lei, H., Niemeijer, A. R., Zhou, Y., & Spiers, C. J. (2022). *Seismic potential of the Anninghe*
980 *Fault zone, southeastern Tibetan Plateau: Constrains from friction experiments on*
981 *natural granite gouge* (No. EGU22-6560). Presented at the EGU22, Copernicus
982 Meetings. <https://doi.org/10.5194/egusphere-egu22-6560>

983 Lockner, D. A., & Byerlee, J. D. (1986). *Open File Report* (Open-File Report).

984 Logan, J. M., Dengo, C. A., Higgs, N. G., & Wang, Z. Z. (1992). Chapter 2 Fabrics of
985 Experimental Fault Zones: Their Development and Relationship to Mechanical

986 Behavior. In *International Geophysics* (Vol. 51, pp. 33–67). Elsevier.
987 [https://doi.org/10.1016/S0074-6142\(08\)62814-4](https://doi.org/10.1016/S0074-6142(08)62814-4)

988 Lu, Z., & He, C. (2014). Frictional behavior of simulated biotite fault gouge under
989 hydrothermal conditions. *Tectonophysics*, 622, 62–80.
990 <https://doi.org/10.1016/j.tecto.2014.03.002>

991 Lu, Z., & He, C. (2018). Friction of foliated fault gouge with a biotite interlayer at
992 hydrothermal conditions. *Tectonophysics*, 740–741, 72–92.
993 <https://doi.org/10.1016/j.tecto.2018.05.003>

994 Luan, F. C., & Paterson, M. S. (1992). Preparation and deformation of synthetic aggregates of
995 quartz. *Journal of Geophysical Research: Solid Earth*, 97(B1), 301–320.
996 <https://doi.org/10.1029/91JB01748>

997 Marti, S., Stünitz, H., Heilbronner, R., Plümper, O., & Drury, M. (2017). Experimental
998 investigation of the brittle-viscous transition in mafic rocks – Interplay between
999 fracturing, reaction, and viscous deformation. *Journal of Structural Geology*, 105, 62–
1000 79. <https://doi.org/10.1016/j.jsg.2017.10.011>

1001 de Meer, S., & Spiers, C. J. (1997). Uniaxial compaction creep of wet gypsum aggregates.
1002 *Journal of Geophysical Research: Solid Earth*, 102(B1), 875–891.
1003 <https://doi.org/10.1029/96JB02481>

1004 Mitchell, E. K., Fialko, Y., & Brown, K. M. (2016). Velocity-weakening behavior of
1005 Westerly granite at temperature up to 600°C. *Journal of Geophysical Research: Solid*
1006 *Earth*, 121(9), 6932–6946. <https://doi.org/10.1002/2016JB013081>

1007 Nakatani, M., & Scholz, C. H. (2004). Frictional healing of quartz gouge under hydrothermal
1008 conditions: 1. Experimental evidence for solution transfer healing mechanism.
1009 *Journal of Geophysical Research: Solid Earth*, 109(B7).
1010 <https://doi.org/10.1029/2001JB001522>

1011 Niemeijer, A. R. (2018). Velocity-dependent slip weakening by the combined operation of
1012 pressure solution and foliation development. *Scientific Reports*, 8(1), 4724.
1013 <https://doi.org/10.1038/s41598-018-22889-3>

1014 Niemeijer, A. R., Spiers, C. J., & Bos, B. (2002). Compaction creep of quartz sand at 400–
1015 600°C: experimental evidence for dissolution-controlled pressure solution. *Earth and*
1016 *Planetary Science Letters*, 195(3–4), 261–275. [https://doi.org/10.1016/S0012-](https://doi.org/10.1016/S0012-821X(01)00593-3)
1017 [821X\(01\)00593-3](https://doi.org/10.1016/S0012-821X(01)00593-3)

1018 Niemeijer, A. R., Spiers, C. J., & Peach, C. J. (2008). Frictional behaviour of simulated
1019 quartz fault gouges under hydrothermal conditions: Results from ultra-high strain
1020 rotary shear experiments. *Tectonophysics*, 460(1–4), 288–303.
1021 <https://doi.org/10.1016/j.tecto.2008.09.003>

1022 Niwa, M., Shimada, K., Aoki, K., & Ishimaru, T. (2016). Microscopic features of quartz and
1023 clay particles from fault gouges and infilled fractures in granite: Discriminating
1024 between active and inactive faulting. *Engineering Geology*, 210, 180–196.
1025 <https://doi.org/10.1016/j.enggeo.2016.06.013>

1026 Okamoto, A. S., Verberne, B. A., Niemeijer, A. R., Takahashi, M., Shimizu, I., Ueda, T., &
1027 Spiers, C. J. (2019). Frictional Properties of Simulated Chlorite Gouge at
1028 Hydrothermal Conditions: Implications for Subduction Megathrusts. *Journal of*
1029 *Geophysical Research: Solid Earth*, 124(5), 4545–4565.
1030 <https://doi.org/10.1029/2018JB017205>

1031 Okuda, H., Niemeijer, A. R., Takahashi, M., Yamaguchi, A., & Spiers, C. J. (2023).
1032 Hydrothermal Friction Experiments on Simulated Basaltic Fault Gouge and
1033 Implications for Megathrust Earthquakes. *Journal of Geophysical Research: Solid*
1034 *Earth*, 128(1), e2022JB025072. <https://doi.org/10.1029/2022JB025072>

1035 Passchier, C., & Trouw, R. A. (1996). *Microtectonics*. *Microtectonics*.
1036 <https://doi.org/10.1007/3-540-29359-0>

1037 Paterson, M. S., & Wong, T. (2005). *Experimental rock deformation--the brittle field* (2nd,
1038 completely rev. and updated ed ed.). Berlin ; New York: Springer.

1039 Rabinowicz, E., & Mutis, A. (1965). Effect of abrasive particle size on wear. *Wear*, 8(5),
1040 381–390. [https://doi.org/10.1016/0043-1648\(65\)90169-9](https://doi.org/10.1016/0043-1648(65)90169-9)

1041 Ree, J.-H. (1994). Grain boundary sliding and development of grain boundary openings in
1042 experimentally deformed octachloropropane. *Journal of Structural Geology*, 16(3),
1043 403–418. [https://doi.org/10.1016/0191-8141\(94\)90044-2](https://doi.org/10.1016/0191-8141(94)90044-2)

1044 Rutter, E. H. (1983). Pressure solution in nature, theory and experiment. *Journal of the*
1045 *Geological Society*, 140(5), 725–740. <https://doi.org/10.1144/gsjgs.140.5.0725>

1046 Rutter, E. H., & Brodie, K. H. (2004a). Experimental grain size-sensitive flow of hot-pressed
1047 Brazilian quartz aggregates. *Journal of Structural Geology*, 26(11), 2011–2023.
1048 <https://doi.org/10.1016/j.jsg.2004.04.006>

1049 Rutter, E. H., & Brodie, K. H. (2004b). Experimental intracrystalline plastic flow in hot-
1050 pressed synthetic quartzite prepared from Brazilian quartz crystals. *Journal of*
1051 *Structural Geology*, 26(2), 259–270. [https://doi.org/10.1016/S0191-8141\(03\)00096-8](https://doi.org/10.1016/S0191-8141(03)00096-8)

1052 Rybacki, E., & Dresen, G. (2004). Deformation mechanism maps for feldspar rocks.
1053 *Tectonophysics*, 382(3–4), 173–187. <https://doi.org/10.1016/j.tecto.2004.01.006>

1054 Sammis, C., King, G., & Biegel, R. (1987). The kinematics of gouge deformation. *Pure and*
1055 *Applied Geophysics*, 125(5), 777–812. <https://doi.org/10.1007/BF00878033>

1056 Schneeberger, R., Mäder, U. K., & Waber, H. N. (2017). Hydrochemical and Isotopic ($\delta^2\text{H}$,
1057 $\delta^{18}\text{O}$, 3H) Characterization of Fracture Water in Crystalline Rock (Grimsel,
1058 Switzerland). *Procedia Earth and Planetary Science*, 17, 738–741.
1059 <https://doi.org/10.1016/j.proeps.2016.12.187>

1060 Scholz, C. H. (1998). Earthquakes and friction laws. *Nature*, 391(6662), 37–42.
1061 <https://doi.org/10.1038/34097>

1062 Scholz, C. H. (2019). *The Mechanics of Earthquakes and Faulting* (3rd ed.). Cambridge
1063 University Press. <https://doi.org/10.1017/9781316681473>

1064 Shea, W. T., & Kronenberg, A. K. (1992). Rheology and deformation mechanisms of an
1065 isotropic mica schist. *Journal of Geophysical Research: Solid Earth*, 97(B11), 15201–
1066 15237. <https://doi.org/10.1029/92JB00620>

1067 Sibson, R. H. (1982). Fault zone models, heat flow, and the depth distribution of earthquakes
1068 in the continental crust of the United States. *Bulletin of the Seismological Society of*
1069 *America*, 72(1), 151–163. <https://doi.org/10.1785/BSSA0720010151>

1070 Simpson, C. (1985). Deformation of granitic rocks across the brittle-ductile transition.
1071 *Journal of Structural Geology*, 7(5), 503–511. <https://doi.org/10.1016/0191->
1072 [8141\(85\)90023-9](https://doi.org/10.1016/0191-8141(85)90023-9)

1073 Smith, S. a. F., Strachan, R. A., & Holdsworth, R. E. (2007). Microstructural evolution within
1074 a partitioned midcrustal transpression zone, northeast Greenland Caledonides.
1075 *Tectonics*, 26(4). <https://doi.org/10.1029/2006TC001952>

1076 Spiers, C. J., Schutjens, P. M. T. M., Brzesowsky, R. H., Peach, C. J., Liezenberg, J. L., &
1077 Zwart, H. J. (1990). Experimental determination of constitutive parameters governing
1078 creep of rocksalt by pressure solution. *Geological Society, London, Special*
1079 *Publications*, 54(1), 215–227. <https://doi.org/10.1144/GSL.SP.1990.054.01.21>

1080 Tenthorey, E., Cox, S. F., & Todd, H. F. (2003). Evolution of strength recovery and
1081 permeability during fluid–rock reaction in experimental fault zones. *Earth and*
1082 *Planetary Science Letters*, 206(1), 161–172. <https://doi.org/10.1016/S0012->
1083 [821X\(02\)01082-8](https://doi.org/10.1016/S0012-821X(02)01082-8)

1084 Tse, S. T., & Rice, J. R. (1986). Crustal earthquake instability in relation to the depth
1085 variation of frictional slip properties. *Journal of Geophysical Research: Solid Earth*,
1086 *91*(B9), 9452–9472. <https://doi.org/10.1029/JB091iB09p09452>

1087 Tullis, J., & Yund, R. (1992). Chapter 4 The Brittle-Ductile Transition in Feldspar
1088 Aggregates: An Experimental Study. In *International Geophysics* (Vol. 51, pp. 89–
1089 117). Elsevier. [https://doi.org/10.1016/S0074-6142\(08\)62816-8](https://doi.org/10.1016/S0074-6142(08)62816-8)

1090 Tullis, J., & Yund, R. A. (1980). Hydrolytic weakening of experimentally deformed Westerly
1091 granite and Hale albite rock. *Journal of Structural Geology*, *2*(4), 439–451.
1092 [https://doi.org/10.1016/0191-8141\(80\)90005-X](https://doi.org/10.1016/0191-8141(80)90005-X)

1093 Twiss, R. J., & Moores, E. M. (1992). *Structural geology*. New York: W.H. Freeman.

1094 Verberne, B. A., Niemeijer, A. R., De Bresser, J. H. P., & Spiers, C. J. (2015). Mechanical
1095 behavior and microstructure of simulated calcite fault gouge sheared at 20–600°C:
1096 Implications for natural faults in limestones. *Journal of Geophysical Research: Solid
1097 Earth*, *120*(12), 8169–8196. <https://doi.org/10.1002/2015JB012292>

1098 Verberne, B. A., Chen, J., Niemeijer, A. R., de Bresser, J. H. P., Pennock, G. M., Drury, M.
1099 R., & Spiers, C. J. (2017). Microscale cavitation as a mechanism for nucleating
1100 earthquakes at the base of the seismogenic zone. *Nature Communications*, *8*(1), 1645.
1101 <https://doi.org/10.1038/s41467-017-01843-3>

1102 Viegas, L. G. F., Archanjo, C. J., Hollanda, M. H. B. M., & Vauchez, A. (2014). Microfabrics
1103 and zircon U–Pb (SHRIMP) chronology of mylonites from the Patos shear zone
1104 (Borborema Province, NE Brazil). *Precambrian Research*, *243*, 1–17.
1105 <https://doi.org/10.1016/j.precamres.2013.12.020>

1106 Visser, H. J. M., Spiers, C. J., & Hangx, S. J. T. (2012). Effects of interfacial energy on
1107 compaction creep by intergranular pressure solution: Theory versus experiments on a
1108 rock analog (NaNO₃): EFFECTS OF INTERFACIAL ENERGY ON CREEP.

1109 *Journal of Geophysical Research: Solid Earth*, 117(B11), n/a-n/a.
1110 <https://doi.org/10.1029/2012JB009590>

1111 Wassmann, S., & Stöckhert, B. (2013). Rheology of the plate interface — Dissolution
1112 precipitation creep in high pressure metamorphic rocks. *Tectonophysics*, 608, 1–29.
1113 <https://doi.org/10.1016/j.tecto.2013.09.030>

1114 Weertman, J. (1978). Creep laws for the mantle of the Earth. *Philosophical Transactions of*
1115 *the Royal Society of London. Series A, Mathematical and Physical Sciences*,
1116 288(1350), 9–26. <https://doi.org/10.1098/rsta.1978.0003>

1117 Wehrens, P., Berger, A., Peters, M., Spillmann, T., & Herwegh, M. (2016). Deformation at
1118 the frictional-viscous transition: Evidence for cycles of fluid-assisted embrittlement
1119 and ductile deformation in the granitoid crust. *Tectonophysics*, 693, 66–84.
1120 <https://doi.org/10.1016/j.tecto.2016.10.022>

1121 Zhang, X., & Spiers, C. J. (2005). Compaction of granular calcite by pressure solution at
1122 room temperature and effects of pore fluid chemistry. *International Journal of Rock*
1123 *Mechanics and Mining Sciences*, 42(7–8), 950–960.
1124 <https://doi.org/10.1016/j.ijrmms.2005.05.017>

1125 Zhang, Xiangmin, Spiers, C. J., & Peach, C. J. (2010). Compaction creep of wet granular
1126 calcite by pressure solution at 28°C to 150°C. *Journal of Geophysical Research: Solid*
1127 *Earth*, 115(B9). <https://doi.org/10.1029/2008JB005853>

1128 Zwingmann, H., Berger, A., Eggenberger, U., Todd, A., & Herwegh, M. (2017). Testing
1129 High-Voltage Electrical Discharges in Disintegrating Claystone for Isotopic and
1130 Mineralogical Studies: An Example Using Opalinus Claystone. *Clays and Clay*
1131 *Minerals*, 65(5), 342–354. <https://doi.org/10.1346/CCMN.2017.064072>

1132 **References From the Supporting Information**

- 1133 Akker, I. V., Kaufmann, J., Desbois, G., Klaver, J., Urai, J. L., Berger, A., & Herwegh, M.
1134 (2018). Multiscale porosity changes along the pro- and retrograde deformation path:
1135 an example from Alpine slates. *Solid Earth*, 9(5), 1141–1156.
1136 <https://doi.org/10.5194/se-9-1141-2018>
- 1137 An, M., Zhang, F., Min, K., Elsworth, D., He, C., & Zhao, L. (2022). Frictional Stability of
1138 Metamorphic Epidote in Granitoid Faults Under Hydrothermal Conditions and
1139 Implications for Injection-Induced Seismicity. *Journal of Geophysical Research:*
1140 *Solid Earth*, 127(3), e2021JB023136. <https://doi.org/10.1029/2021JB023136>
- 1141 Berg, S., Kutra, D., Kroeger, T., Straehle, C. N., Kausler, B. X., Haubold, C., et al. (2019).
1142 ilastik: interactive machine learning for (bio)image analysis. *Nature Methods*, 16(12),
1143 1226–1232. <https://doi.org/10.1038/s41592-019-0582-9>
- 1144 Blanpied, M. L., Lockner, D. A., & Byerlee, J. D. (1995). Frictional slip of granite at
1145 hydrothermal conditions. *Journal of Geophysical Research: Solid Earth*, 100(B7),
1146 13045–13064. <https://doi.org/10.1029/95JB00862>
- 1147 Dinnebier, R. E., & Billinge, S. J. L. (Eds.). (2008). *Powder diffraction: theory and practice*.
1148 Cambridge: Royal Society of Chemistry.
- 1149 Kanit, T., Forest, S., Galliet, I., Mounoury, V., & Jeulin, D. (2003). Determination of the size
1150 of the representative volume element for random composites: statistical and numerical
1151 approach. *International Journal of Solids and Structures*, 40(13–14), 3647–3679.
1152 [https://doi.org/10.1016/S0020-7683\(03\)00143-4](https://doi.org/10.1016/S0020-7683(03)00143-4)
- 1153 Lei, H., Zhou, Y., Yao, W., Ma, X., He, C., Dang, J., et al. (2022). Earthquake nucleation
1154 conditions of Anninghe Fault constrains from frictional experiments on natural granite
1155 gouge. *Chinese Journal of Geophysics*, 65(3), 978–991.
1156 <https://doi.org/10.6038/cjg2022P0248>
- 1157 Lockner, D. A., & Byerlee, J. D. (1986). *Open File Report* (Open-File Report).

1158 Mitchell, E. K., Fialko, Y., & Brown, K. M. (2016). Velocity-weakening behavior of
1159 Westerly granite at temperature up to 600°C. *Journal of Geophysical Research: Solid*
1160 *Earth*, 121(9), 6932–6946. <https://doi.org/10.1002/2016JB013081>

1161 Okuda, H., Niemeijer, A. R., Takahashi, M., Yamaguchi, A., & Spiers, C. J. (2023).
1162 Hydrothermal Friction Experiments on Simulated Basaltic Fault Gouge and
1163 Implications for Megathrust Earthquakes. *Journal of Geophysical Research: Solid*
1164 *Earth*, 128(1), e2022JB025072. <https://doi.org/10.1029/2022JB025072>

1165 Rietveld, H. M. (1969). A profile refinement method for nuclear and magnetic structures.
1166 *Journal of Applied Crystallography*, 2(2), 65–71.
1167 <https://doi.org/10.1107/S0021889869006558>

1168